Energy Storage Materials 81 (2025) 104434

Contents lists available at ScienceDirect

Energy Storage Materials

journal homepage: www.elsevier.com/locate/ensm

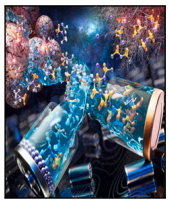

Understanding the effect of vinylene carbonate on SEI formation, morphology and stability on lithium metal anodes

Janika Wagner-Henke [a], Dacheng Kuai [b], Perla B. Balbuena [c], Ulrike Krewer [a,*]

[a] Institute for Applied Materials - Electrochemical Technologies, Karlsruhe Institute of Technology, Adenauerring 20b, Karlsruhe, 76131, Germany
[b] Department of Chemical Engineering and Department of Chemistry, Texas A&M University, College Station, 77843, TX, United States
[c] Department of Chemical Engineering, Department of Chemistry and Department of Materials Science and Engineering, Texas A&M University, College Station, 77843, TX, United States

ARTICLE INFO

Dataset link: https://doi.org/10.35097/jyg9f6admdh8a5s2

Keywords:
Solid electrolyte interphase
Vinylene carbonate
Lithium metal battery
Kinetic Monte Carlo

ABSTRACT

Lithium metal batteries are promising for applications requiring high energy density storages, but their practical implementation is hindered by the high reactivity of metallic lithium with liquid electrolytes. Film-forming additives can contribute to stabilize the lithium/electrolyte interface by promoting a well-performing solid-electrolyte interphase (SEI). However, their specific influence on SEI formation mechanisms remains poorly understood, causing challenges in designing advantageous SEIs. In this work we reveal the role of the widely used electrolyte additive vinylene carbonate (VC) in SEI formation on lithium metal. An ab initio informed kinetic Monte Carlo approach is applied to bridge the gap between atomistic simulations and the timescale of seconds, enabling the first mechanistic investigation of VC-driven SEI growth beyond elementary reaction steps. We find that VC only significantly impacts SEI formation beyond the millisecond range with only a minor impact on the previous formation of the inorganic passivation layer close to the anode surface. Yet, it enables a chemically-driven polymerization process, passivating the surface without ongoing consumption of lithium. The resulting polymeric layer prevents dissolution of SEI and intermediate species and stops the continuous consumption of electrolyte species. Higher VC concentrations do not significantly alter the protective mechanism but result in a higher proportion of remaining additive, allowing for repassivation during operation. Overall, this study provides an in-depth molecular understanding of the influence of VC on SEI formation, paving the way to model-assisted SEI design.

1. Introduction

Reliable, safe and high-energy density energy storage systems are a crucial technology in the transition towards a fossil-free and climate-friendly future. Today's lithium-ion batteries already meet the requirements for a variety of different applications such as consumer electronics, power tools or electric vehicles [1]. However, there is still the urgent demand for battery technologies with increased energy-densities to allow for e.g. long-range electric vehicles or electric propulsion in aviation [2,3]. In this context, lithium-metal electrodes are considered very promising, because of their high theoretical capacity of 3860 mAh g^{-1} [4]. However, their high reactivity also causes challenges when it comes to application. It makes the lithium metal/electrolyte interface difficult to control and may cause uncontrolled electrolyte degradation including thermal runaway, ongoing loss of active material and dendrite growth [5,6]. Hence, the stabilization of this interface is crucial to enable safe and long-lasting lithium-metal batteries (LMB).

One strategy to achieve such stabilization is the use of interphase forming electrolyte additives [5,7]. These can positively alter the properties of the SEI, e.g. making it thinner, more electrically passivating and/or more mechanically stable against electrode volume changes [5,7]. A popular additive for both, lithium-ion batteries and LMB is VC [7,8]. It is well-known to improve the cyclic efficiency of lithium-metal-based batteries [9–11] and is reported to form a mechanically stable polymeric surface film, which may also increase the internal resistance of the LMB cells [8,9,11,12]. In recent years, advanced cryo-transmission electron microscopy studies could reveal that VC in carbonate-based electrolytes leads to a mosaic-like SEI on electrochemically deposited lithium, consisting of inorganic species embedded in organic SEI layers [9]. Furthermore, it could be shown that VC has a substantial impact on the initial SEI formation on lithium metal before any external potential is applied. It was shown to cause a better passivation of the surfaces and decrease the overall height of the formed

* Corresponding author.
E-mail address: ulrike.krewer@kit.edu (U. Krewer).

https://doi.org/10.1016/j.ensm.2025.104434
Received 6 May 2025; Received in revised form 20 June 2025; Accepted 28 June 2025
Available online 12 July 2025

SEI [13]. However, to gain a mechanistic understanding of the specific influence of VC on SEI formation, theoretical studies are required. To date, most contributions in this field apply first principles density functional theory (DFT) and have focused on identifying possible degradation and polymerization pathways [14–20]. Notably, Kuai et al. [20] recently conducted an in-depth DFT investigation of VC decomposition and polymerization in an EC-based electrolyte close to the lithium metal surface. This study provides reaction activation barriers and reaction energies along with possible degradation and polymerization mechanisms and provides a good understanding of the molecular-level interactions between VC, EC and Li^+ ions. However, due to the high computational cost, first principles studies are inherently limited to short timescales and small system sizes. As a result, they cannot capture the full evolution of the SEI layer.

Kinetic Monte Carlo (kMC) models are a promising approach to overcome these limitations [21]. The stochastic method models the dynamic evolution of a system as a sequence of randomly selected rare events, e.g. (electro-)chemical reactions or transport processes, while neglecting fast processes such as atomic vibrations [22,23]. This allows kMC models to significantly increase reachable length- and timescales of the simulation, while maintaining a molecular resolution of the results [24]. However, in contrast to DFT or other first principles methods, kMC requires prior knowledge of the system to define relevant rare events and the corresponding rate probabilities [23]. These information are commonly derived from experiment or first principles calculation techniques such as DFT [23,25]. In recent years, various research groups have started to apply this simulation method to surface phenomena in batteries. The corresponding research questions range from the transport and intercalation of Li^+-ions [26] over dendrite formation in LMB [27] to SEI formation on graphite for lithium ion batteries [28–32] or on hard carbon for sodium-ion cell [33] during the first charging cycle. Lately, a 3-dimensional kMC framework has been developed that enables simulating the initial SEI formation on lithium metal surfaces [34,35]. So far, all of the above-mentioned models have only been applied to very simple electrolyte systems and did not consider the effect of additives. Since VC is well known to form polymers [8,36,37], an extension of the existing kMC frameworks by polymerization is required to study its effect on SEI formation. There are examples from classical polymer-science in which kMC approaches were applied to study different polymer properties such as chain length distribution or the order of copolymers [38–42]. In many cases, the focus was on bulk-phase polymerization, which is why off-lattice approaches were chosen that do not save any configurational information [38–40]. However, some works also focused on surface-initiated polymerization and applied lattice-based kMC approaches [41,42].

Building on these efforts, we present the first kMC model of SEI formation that explicitly accounts for polymerization reactions. This allows us to capture the formation of polymeric SEI components and to assess the impact of the electrolyte additive VC on the SEI formation on lithium metal beyond elementary reaction steps. The study provides new insights into how VC plays its role as an SEI-forming additive, how it causes a better cycling efficiency and what the major processes of the polymer film formation are. Additionally, the study bridges the scales from the ns range of DFT and molecular dynamics simulations to the macroscopic scale of seconds.

2. Results and discussion

2.1. Electrolyte degradation reactions

This study focuses on the effect of the electrolyte additive VC on the SEI formation in the simple baseline electrolyte ethylene carbonate (EC) + 1.2M $LiPF_6$. Since all electrolyte species may in principle contribute to SEI formation, we identified the major degradation pathways for each electrolyte component based on literature data and DFT calculations. The degradation reactions as well as the related kinetic parameters for the electrolyte solvent EC and the conductive salt $LiPF_6$ were identified in a previous publication [35] and are adopted for this study (cf. SI Fig. 1 and SI Tab. 2). The current literature on the degradation of VC on anode surfaces suggests multiple degradation and polymerization mechanisms. The two major possibilities which are frequently reported are the ring-opened polymerization of VC [14,18,43] and the polymerization without ring-opening which leads to the formation of poly(VC) [44–48]. Products of both reaction pathways have been experimentally identified as components of VC-derived SEI layers on graphite anodes [49]. In order to clarify, which mechanism is kinetically preferred, Kuai and Balbuena [20] recently conducted an extensive DFT study for both VC polymerization mechanisms as well as for EC polymerization and cross-polymerization between both species. Based on this study, we identified the poly(VC)-formation initiated by a reduced VC-molecule and the cross-polymerization with an EC-based initiating radical as energetically favorable reaction mechanisms. Both mechanisms are summarized in Scheme 1. Details on this selection may be found in the Section 4.

Besides the aforementioned initiation and propagation mechanisms, termination reactions are an important step of each polymerization process. Based on the radical species that are present in our system, namely $(Li^+)VC^{\bullet -}$, $(Li^+)EC^{\bullet -}$, $(Li^+)poly(VC)_n^{\bullet -}$, $(Li^+)poly(EC/VC)_n^{\bullet -}$, we defined the following five recombination processes to be added to our reaction network: The recombination of two VC radicals (T1), the recombination of a VC radical and an EC radical (T2), the recombination of two active chain ends (T3), the recombination of an active chain end with an EC radical (T4), and the recombination of an active chain end with a VC radical (T5). Additionally, the recombination of two EC radicals is accounted for by the Lithium Ethylene Dicarbonate (LiEDC) forming reaction (R3), which has been parameterized as part of a previous study [23]. The chemical structures and corresponding reactions which were used to parameterize these processes by DFT calculations are summarized in Scheme 2. Details on the calculation and kinetic parameters may be found in Section 4 and Table 3.

2.2. Primary SEI formation on the microsecond timescale

To analyze the effect of the VC additive on the primary SEI formation on lithium metal in a 1.2M $LiPF_6$/ EC electrolyte, 5 wt% of VC were added to the electrolyte in the initial simulation box. A previous work demonstrated that during the initial SEI formation on the nanosecond to microsecond scale, the assumption of Li^+-coordinated electrolyte molecules (hereafter referred to as 'lithiated') aligns well with the local conditions on the lithium metal surface [35]. Consequently, for the subsequent calculations, we applied the parameter set for the lithiated case (cf. Section 4). It should be further noted that in the following analysis for simplicity, the term 'polymer' refers to all macromolecules composed of at least two VC and/or EC monomers. Moreover, all simulated parameter sets may be found in SI Tab. 5 and are subsequently referred to as cases.

The SEI formed 2 μs after the initial contact of lithium metal and the liquid electrolyte phase is displayed in Fig. 1. Fig. 1 (a) and (b) show the overall species distribution and SEI composition for the electrolyte without (left) and with (right) VC, respectively. The primary SEI formed in EC + 1.2M $LiPF_6$ within the first 2 μs is inorganic and consists of two layers: A Li_2CO_3-layer closer to the lithium metal surface and a LiF-layer above. In the VC-containing electrolyte, we observe the additional formation of an organic/polymeric layer above the inorganic SEI. Interestingly, the formed inorganic layer barely differs from the layer formed in the additive-free electrolyte. The only significant effect is that the LiF peak in Fig. 1 (b) is slightly decreased for the VC-containing electrolyte case. From this it can be concluded that VC suppresses the salt degradation during the initial SEI formation to a certain extent. Fig. 1 (c) further shows the height evolution of the SEI for the electrolyte compositions with and without VC within the first

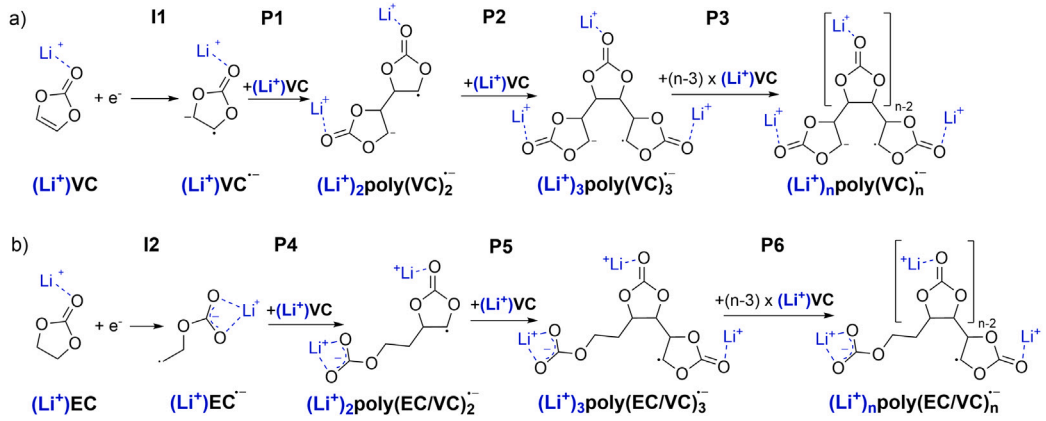

Scheme 1. Considered polymerization mechanisms with optional Li^+-coordination shown in blue. (a) poly(VC)-formation mechanism. (b) Cross-polymerization mechanism with EC radical as initiator.

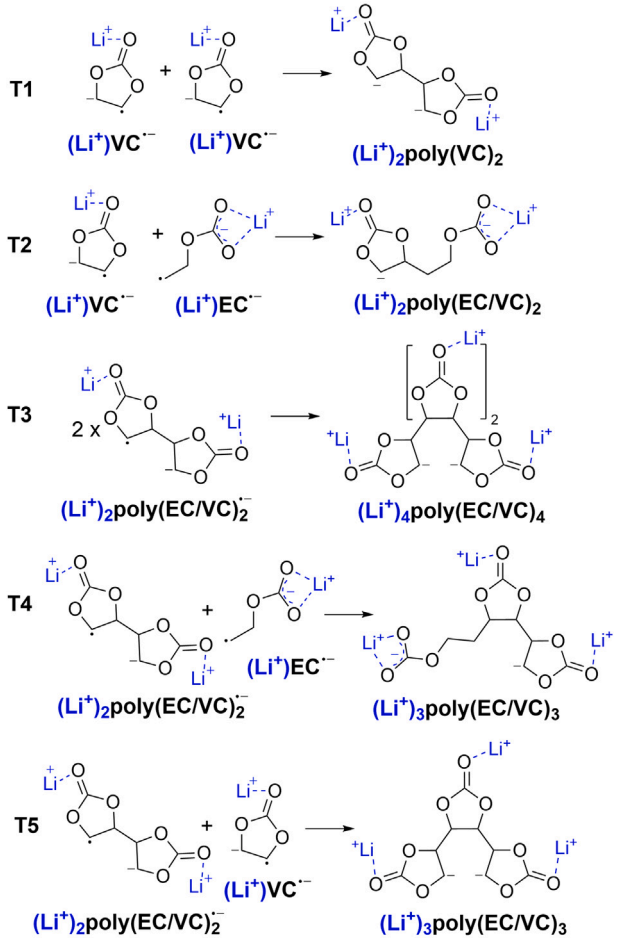

Scheme 2. Considered termination reactions for the DFT-based energy calculation with optional Li^+-coordination shown in blue.

2 μs. The overall trajectory of the SEI growth is very similar in both cases with a steep increase of the SEI height within the first ns and a continuous deceleration of the SEI growth afterwards, which can be attributed to the increasing passivation of the lithium metal surface. However, over time, we observe an increasing spread between the SEI height evolution of both systems, with the VC-containing electrolyte leading to a slightly thicker primary SEI than the VC-free electrolyte. This can be attributed to the formation of the additional polymer layer. 2 μs after the contact of electrolyte with lithium, the average height of the SEI results in 5.18 nm with VC and in 4.64 nm without VC in the electrolyte. At first glance, this result is not as expected since it contradicts the experimental findings by Weber et al. [13], who investigated the SEI thickness evolution on lithium foil in 1M $LiPF_6$ in EC:EMC (1:1 v/v) with and without 5% VC and found a thicker SEI in the VC-free electrolyte. The authors attribute this to the formation of decomposition species that are only loosely associated with the electrode surface and thus only provide limited surface passivation. However, it is important to note that these experimental measurements were conducted on significantly longer timescales, ranging from minutes to hours and are hence not directly comparable to the presented simulation results on

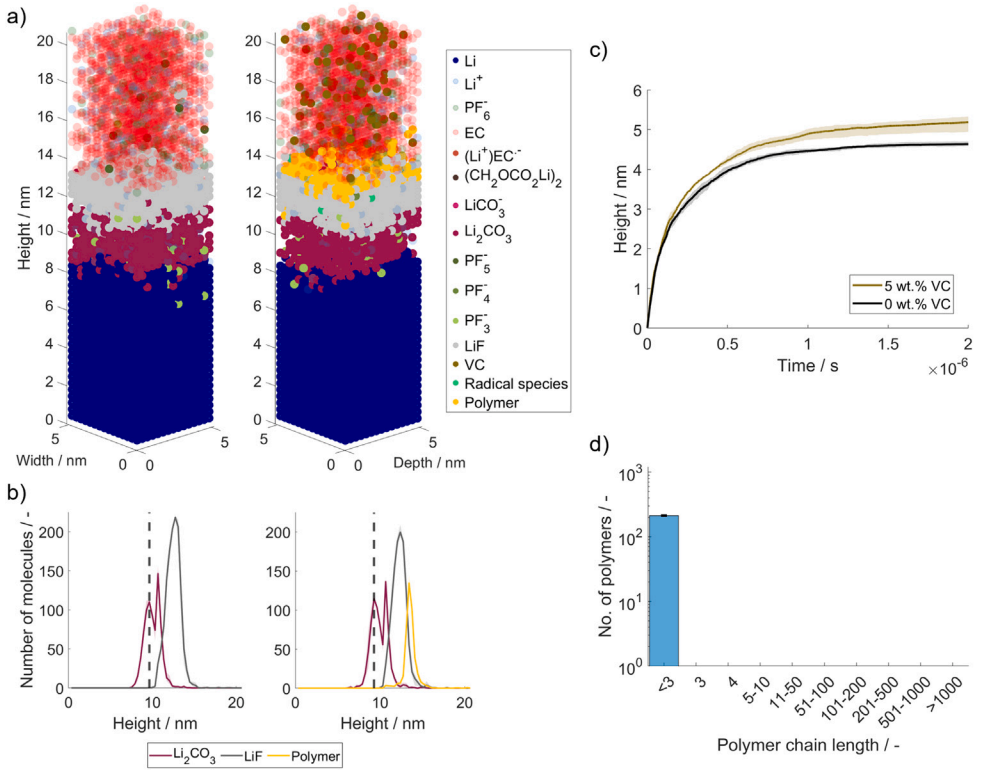

Fig. 1. SEI formation in carbonate-based electrolyte with (case 1, cf. SI) and without (case 2, cf. SI) 5 wt% VC after the first 2 μs. The results in (a) are based on a single kMC run and the results in (b)–(d) display the average of three runs with the same parameter set. Deviations from the average are represented as shadings around the average in (b) and (c). In (d), they are illustrated using error bars. (a) SEI composition and morphology without (left) and with (right) VC. (b) SEI species distribution over height without (left) and with (right) VC. The dashed line represents the upmost layer in which metallic lithium is present after 2 μs. (c) Evolution of SEI height up to 2 μs for both cases. (d) Polymer chain length distribution in SEI formed in VC-containing electrolyte after 2 μs.

the microsecond timescale. The observed discrepancies may arise from slow processes such as the dissolution of electrolyte decomposition products and secondary reactions of dissolved intermediates, which are likely to contribute to the experimental observations but only occur on longer timescales and are thus not yet captured by the simulation model.

A more detailed analysis of the polymeric layer formed in the VC-containing electrolyte is presented in Fig. 1 (d), which displays the chain length distribution of the polymer species in the VC-containing case. It reveals that the observed organic layer does not consist of actual macromolecules. Instead, within the considered time frame, only dimers have formed. The explanation of this observation is twofold. First, the pristine lithium metal surface, which is present at the beginning of the simulation, is very reactive. This favors many reduction reactions and hence the formation of many VC radicals, which can act as initiators for the subsequent polymer propagation. Yet, due to the high reactivity, the local concentration of these radical species is high, which leads to quick recombination and hence to the formation of inactive dimers. Second, the energy barriers of the propagation reactions P1–P6 in the lithiated parameter set range between 9.97 and 14.1 kcal mol^{-1} (cf. Table 3). This translates to average reaction times of 2 μs up to 2.2 ms, which is higher than the here investigated timescale. We therefore expect that a significant number of propagation reactions can only be observed on a considerably larger timescale.

Overall, VC only has a limited effect on the formation of the initial inorganic SEI up to the lower μs-timescale. The slight suppression of salt decomposition and the formation of an additional organic layer might not be sufficient to justify the performance improvement of lithium anodes which is observed experimentally. Furthermore, the observation of an even thicker SEI formed from the VC-containing electrolyte compared to the VC-free electrolyte and the exclusive formation of dimers contradicts experimental findings. We therefore conclude that key effects of the VC additive become apparent only on significantly longer timescales. Therefore, in order to understand the actual working principles of the VC additive, an analysis at longer timescale is conducted in the following.

2.3. SEI formation beyond the microsecond timescale

Simulation of SEI growth up to milliseconds or seconds with the same approach as in Section 2.2, would cause prohibitively high computational costs, and thus runtime. Therefore, in order to reach simulations at much longer time scales and acceptable runtimes, the kMC time steps may be increased by identifying quasi-steady state processes that can be removed from the kMC simulations. In our subsequent simulations we take advantage of the fact that after the first microsecond, the electrolyte species are homogeneously distributed above the densest SEI layer (cf. SI Fig. 4 (c) and (d)). Hence, the further SEI formation is not transport-limited and transport processes can be considered to be quasi-stationary. As a consequence, for timescales exceeding 2 μs, all electrolyte species (EC, $LiPF_6$ and VC) are considered implicitly, i.e. through a residence probability derived from their respective bulk concentrations (cf. Equation 6). Moreover, in contrast to our short-term calculations, we further initialize our long-time calculations with a reduced initial SEI consisting of a dense LiF-film of varying thicknesses, to represent the primary passivation layer that has been formed upon the first contact of lithium metal with the electrolyte. Details on the assumptions for the long-time calculations may be found in Section 4 and in SI Sec. 1.5. Overall, this allows us to increase the simulation time from the microsecond- up to the second-timescale and above.

Fig. 2 (a) shows the temporal evolution up to 1 s of the SEI composition and morphology in the VC-containing electrolyte EC + 1.2M $LiPF_6$ + 5 wt% VC. Here, the thickness of the initial passivation layer is set to 3.57 nm. This corresponds to the observed distance between

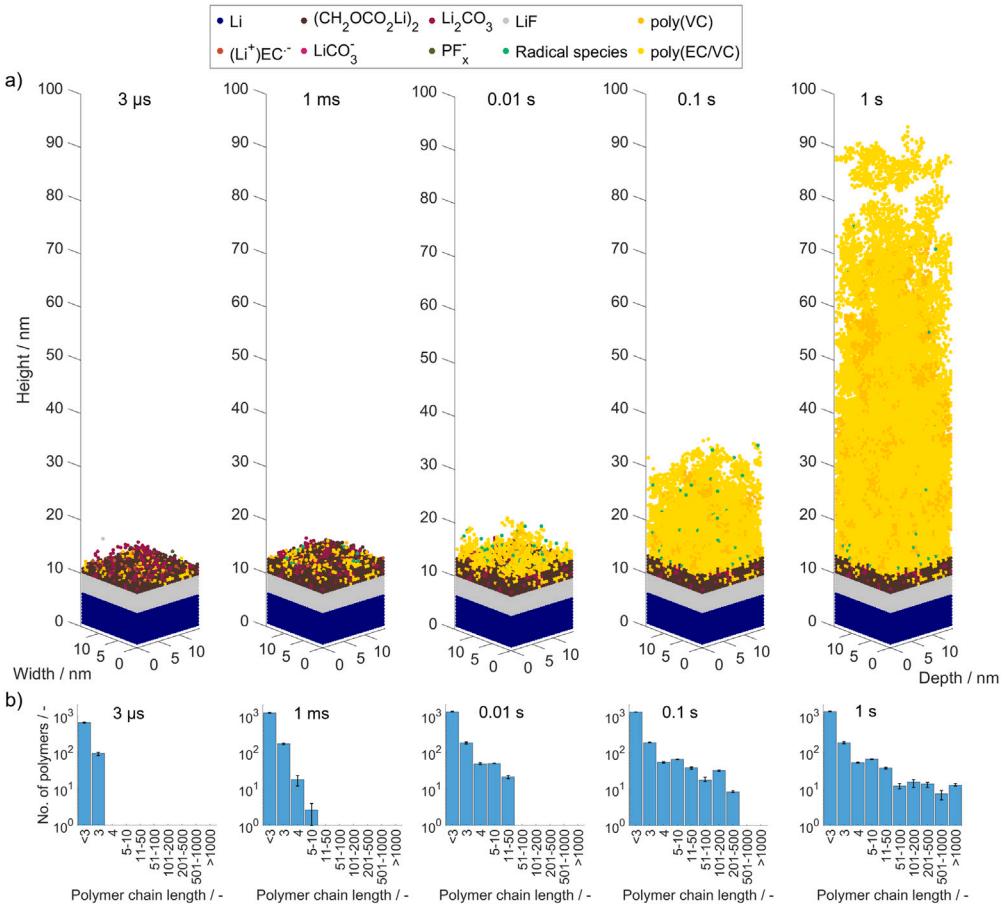

Fig. 2. Temporal evolution of SEI growth on lithium metal in EC + 1.2M $LiPF_6$ + 5 wt% VC until 1 s after formation of an initial 3.57 nm thick, dense LiF-based SEI at 2 µs (case 3, cf. SI). (a) Spatial morphology and composition of the formed SEI at different times. (b) Corresponding chain length distribution of the formed polymer species.

the upmost metallic lithium and the densest layer of the primary SEI after 2 µs (cf. Fig. 1 b). For any electrochemical reaction to occur after 2 µs, electrons need to bridge at least this distance. The first box shows the configuration after a total time of 3 µs after the initial contact between lithium and the electrolyte, since the initially placed LiF-layer represents the primary SEI after 2 µs (cf. Section 2.2). On the microsecond-scale we observe the formation of a comparatively dense layer consisting of a mixture of LiEDC, Li_2CO_3 and different polymeric species and the formation of small Li_2CO_3 clusters above the surface inside the electrolyte phase. The polymer chain length distribution in Fig. 2 (b) demonstrates that up to 3 µs no chain formation with more than three units occurs. This finding is well in line with the previous observation made in the short-term kMC simulation (cf. Section 2.2). The composition of the dense layer differs from the short-term simulations as a consequence of the comparatively low local Li^+ ion concentration in the bulk phase of the electrolyte. This leads to changed reaction kinetics and the additional formation of the organic LiEDC.

Up to 1 ms, the dense organic layer has slowly grown. Moreover, additional short chains with a chain length up to 3 have formed. Overall, the vast majority of oligomer species still has a chain length of 2 or 3, and only few longer chains with a maximum chain length of 5 – 10 units are present. The picture changes when further increasing the timescale to multiple ms. 10 ms after the first contact of lithium and electrolyte, an increase in polymeric species can be clearly seen in Fig. 2 (a). Moreover, the corresponding chain length distribution in Fig. 2 (b) indicates the formation of an increasing number of longer chains with more than 10 units. This trend persists on larger timescales. At 0.1 s we can observe that the polymer species have significantly grown towards the electrolyte phase and thereby form a porous polymer layer on top of the initial SEI with increased chain length. The developing polymer layer consists of a mixture of poly(VC) species and poly(EC/VC) species. In the latter, an EC radical species has acted as initiator. Overall, the EC-radical based polymers constitute the majority of the polymeric SEI. Interestingly, the previously formed Li_2CO_3 clusters close to the surface are gradually encapsulated by the growing polymer phase. This observation aligns well with cryo-TEM measurements reported in literature, which show the formation of inorganic species embedded within organic SEI layers [9].

1 s after the initial contact of lithium and electrolyte, the surface is completely covered with a thick polymer layer consisting of both, poly(VC) and poly(EC/VC) chains. In contrast, the Li_2CO_3- and LiEDC-based SEI-layer has not further grown and remains unchanged in its properties. We attribute this to passivating and protective properties of the formed polymeric layer. It prevents continuous reductive decomposition of electrolyte components and active material, while it itself is formed through a purely chemical process. Moreover, we observe that the number of shorter polymer chains with up to 10 units almost remained constant, i.e. they were not reactive and only few chains have grown into long polymer chains with several hundred up to more than 1000 units. An explanation on this phenomenon is provided below in the discussion on Figs. 4 and 5. We can further conclude that the polymer growth is still ongoing and that, for times longer than 3 µs, the chain propagation represents, by far, the most prevalent process, accounting for over 99% of the occurrences (cf. SI Fig. 12 (a)). As the growth has not yet stopped, we cannot conclude on the final thickness of the VC-based SEI. However, the average height of the formed SEI after 1 s can be observed to be quite large with 72.2 nm, which is in the range of experimentally observed SEI thicknesses in VC-containing

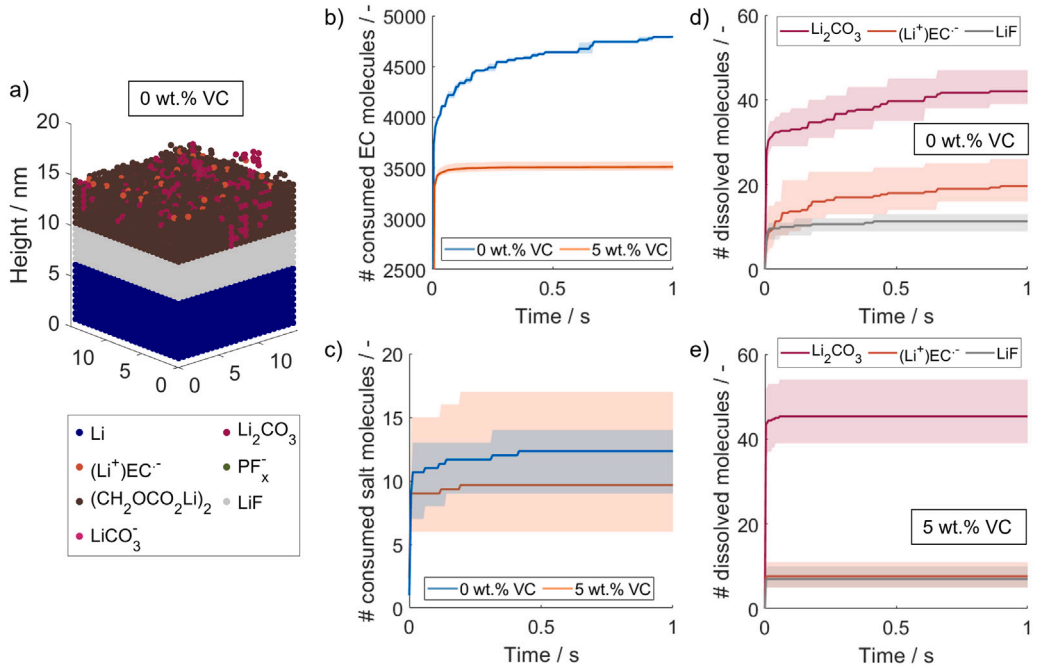

Fig. 3. Comparison of long-time SEI formation in VC-free (case 4, cf. SI) and VC-containing (case 3, cf. SI) electrolyte. (a) SEI composition and morphology in VC-free electrolyte after 1 s. (b) Comparison of consumed EC molecules over time. (c) Comparison of consumed salt molecules over time. (d) Number of dissolved electrolyte decomposition products over time in VC-free electrolyte. (e) Number of dissolved electrolyte decomposition products over time in VC-containing electrolyte.

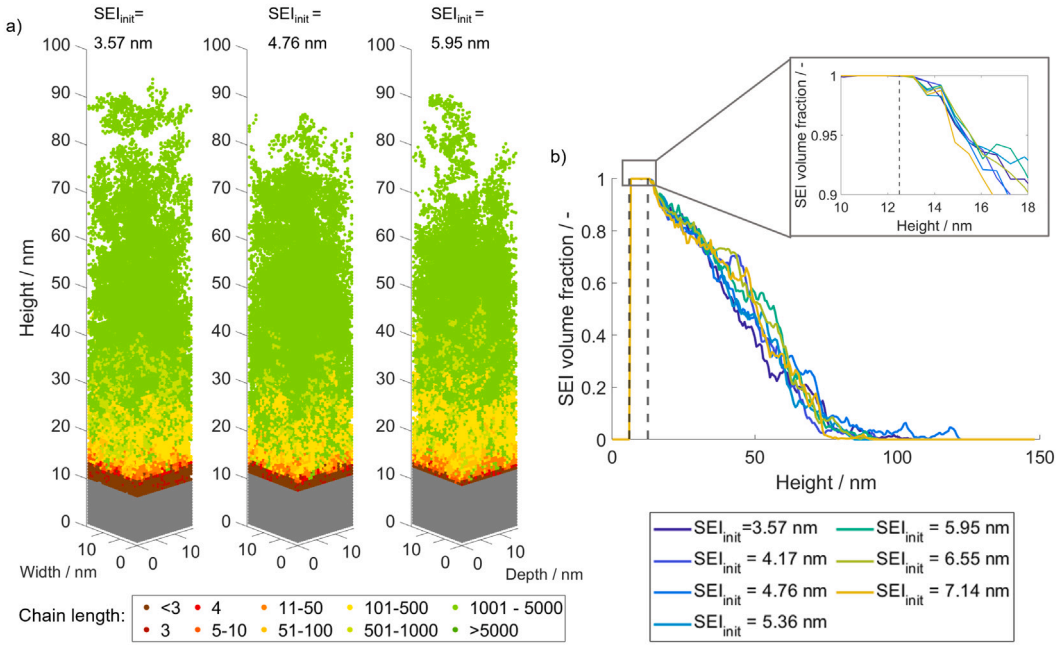

Fig. 4. Polymeric SEI layer formed after 1 s for varying thicknesses of the initial LiF passivation layer between 3.57 nm and 7.14 nm (cases 3, 5, 6, 7, 8, 9, 10, cf. SI). (a) Spatial polymer chain length distribution (cases 3, 6, 8, cf. SI). (b) SEI volume fraction over height (cases 3, 5, 6, 7, 8, 9, 10, cf. SI). The left dashed line represents the lithium metal surface and the right dashed line the highest completely dense passivation layer.

systems [13] or slightly above [9]. Uncertainties in this result may occur due to the hard-to-determine long chain propagation kinetics. While minor alterations in this rate do not affect the system dynamics in a way that the observed SEI composition or morphology changes, it influences the duration of layer formation (cf. SI Fig. 13). Hence, while the observed trends are robust, the time-dependent thickness should be interpreted with caution.

A deeper understanding of how VC impacts the SEI formation is gained by comparing the long-time formation in the VC-containing and in the VC-free electrolyte. Fig. 3 (a) shows the formed SEI after 1 s in the VC-free electrolyte. It can be observed that the formed SEI mostly consists of the organic LiEDC mixed with some clusters of Li_2CO_3. Overall, the layer is significantly thinner than the SEI that formed within the first second in the VC-containing electrolyte (cf. Fig. 2). The

major reason for this is the missing polymer layer. This observation contradicts previous experimental literature, which reported that the VC-containing electrolyte leads to a significantly thinner SEI than the VC-free electrolyte [13].

A closer examination of electrolyte consumption and the number of dissolved species provides a better understanding of these differences between simulation and experiment and the effect of the VC additive. First, Figs. 3 (b) and (c) show that a significantly higher amount of the electrolyte solvent EC is consumed within the first second in the VC-free compared to the VC-containing electrolyte. A similar but less distinct trend is observed for $LiPF_6$. Moreover, the consumption of EC is still ongoing in the VC-free electrolyte case, whereas it has stopped after approximately 0.2 s in the VC-containing electrolyte. A similar trend may be observed in Fig. 3 (d) and (e), which show the number of dissolved electrolyte decomposition products over time. We here define a dissolved species as a species that either leaves the kMC box through its open upper boundary or that has moved more than 5 nm away from the highest SEI (cf. Section 4.2)). It should be noted that this does not include the dissolution of previously deposited and clustered SEI species, which is due to the short timescale below 1 s not considered in our model. It might, though, play a significant role at longer times [33] - this holds especially for the VC-free electrolyte. Instead we only account for not yet deposited electrolyte decomposition products that stay and diffuse in the electrolyte, rather than deposit and cluster on the surface. An advanced approach for modeling SEI solubility is currently under development. In both, the VC-free and VC-containing electrolyte, dissolved Li_2CO_3, LiF and $(Li^+)EC^{\bullet-}$ can be observed. However, a significantly higher amount of LiF and $(Li^+)EC^{\bullet-}$ stays in solution in the VC-free electrolyte, while the overall number of dissolved Li_2CO_3 molecules after 1 s is similar. The number of dissolved molecules still increases in the VC-free electrolyte after 1 s, while it remains constant after a few milliseconds in the VC-containing electrolyte. The dissolved electrolyte decomposition products may undergo further subsequent reactions and/or form solid clusters, which are only loosely connected to the surface. Thus, they could form a porous layer which is still part of the SEI but does not adequately passivate the surface to prevent further reduction of the electrolyte. Similar mechanisms have been previously proposed by other kMC studies for graphite anodes [29,32] and hard carbon anodes for Na-ion batteries [33]. SEI dissolution on lithium metal anodes has also been observed experimentally for different electrolyte chemistries [50–52]. Although the observed number of dissolved molecules does not quantitatively explain the difference between simulation within the first second and the experimental observations of Weber et al. [13], our simulation results suggest the following qualitative explanation: The VC-free electrolyte does not passivate the lithium metal surface in a way that sufficiently suppresses ongoing electrolyte reduction and dissolution of electrolyte decomposition products. This irreversibly consumes active material and electrolyte components. In contrast, VC quickly passivates the surface against ongoing electrolyte decomposition within the first 0.2 s after contact. Importantly, this primarily occurs through chemical propagation rather than electrochemical reactions and hence consumes significantly less active material, i.e. lithium. We further hypothesize that the formed polymer chains constitute a comparatively stable SEI, which does not dissolve to a significant extent.

Further insights into the effect of the additive VC are subsequently provided by the analysis of the spatial chain length distribution and height-depending porosity of the polymeric SEI. Thereby, the thickness of the initial passivation layer is varied to study the effect of varying degrees of initial passivation, which can e.g. be caused by different native or artificial passivation layers on the lithium metal surface [53–56]. Fig. 4 (a) depicts the height-dependent polymer chain length distribution for a varying thickness of the initial LiF layer between 3.57 and 5.95 nm. Interestingly, we observe many short chains closer to the electrode and a constant increase of the chain length towards the electrolyte phase independent of the thickness of initial passivation. Thereby, the polymeric phase in close proximity to the lithium metal consists exclusively of dimers. This effect is most distinct for thinner initial passivation layers and diminishes the thicker the initial layer gets. Fig. 4 (b) further shows that this dimeric part of the SEI is completely dense without any porosity. Together with the initial LiF-layer this leads to an overall dense passivation layer with a thickness of approximately 6.55 nm for all investigated cases. Above this height, the porosity of the SEI gradually increases with the distance to the lithium electrode. From this, we conclude that a minimum passivation of the lithium surface is required before longer polymer chains can form and that the subsequent polymer layer is more porous. The reason is that without sufficient passivation the rate of electron transport through the SEI and subsequent reduction of electrolyte and additive species to radicals is still higher than the propagation rate. Hence, close to the surface the local concentration of radicals is high, which favors recombination reactions and therefore the formation of dimers. It should be noted that the thickness of this dense layer depends on the electron transport through the formed SEI – a better passivating SEI will lead to a thinner dense layer and vice versa.

The previous observation on spatial polymer chain length distributions is supported by the analysis of the spatial and temporal evolution of radicals and reactive chain ends (summarized as radical species). Fig. 5 (a) displays the number of free and blocked radicals and their sum for an initial passivation layer with a thickness of 3.57 nm. The term ‘blocked radicals’ describes radical species which are fully embedded inside the polymer layer and hence have a low chance to get in contact and react with fresh monomer species or other radical species. In our simulation we interpret a radical species to be blocked, if all neighboring sites are occupied by SEI species. In contrast ‘free radicals’ refers to radical species which are still capable to further propagate as electrolyte can reach the respective sites. Most radicals are formed early within the first 0.2 s after the contact with the electrolyte. Subsequently, the total amount of radical species remains almost constant with only minor fluctuations. The reason for this is twofold. First, the increasing surface passivation due to polymer growth limits the number of electron transfer reactions and hence the ongoing electrolyte degradation which would be required for the formation of new radical species. Second, only very few termination reactions occur that could decrease the overall amount of radical species. This is because the number of free radicals steadily decreases over time and slowly approaches zero, while the number of blocked radicals increases and approaches the overall number of radical species. Free radicals are thus converted into blocked ones, which can no longer reach other radical species and can hence not undergo termination reactions. The distribution of radicals over height after 1 s in Fig. 4 (b) further reveals that most radical species are located relatively close to the electrode surface, where they were formed through reduction reactions. Only few radical species can be found further away from the electrode. This correlates well with our previous observation that only few long polymer chains grow into the electrolyte phase (cf. Fig. 4). The major reason for this is that most radicals or reactive chain ends get encapsulated within the polymer phase and hence get shielded from fresh monomer species and from further propagation reactions. Similar effects have been previously reported in studies from polymer-science focusing on surface-induced polymerization [41,42,57–61]. They are usually known as confinement effects that shield or hinder initiators [57–59] and reactive chain ends [41,42,58] from propagation. Here, to the best of our knowledge, we observe this effect for the first time in relation to SEI. This confinement effect leads to an increased number of termination reactions between confined radical species within the polymer layer [57]. In our simulations, polymers and thus reactive chain ends cannot move towards each other to recombine. Yet, similarly as the terminated polymers, the hindered chain ends do not participate in further propagation reactions. Thus, the simulation indeed reproduces the shielding effect. Overall, the shielding effect significantly slows down the SEI growth over time (cf. SI Fig. 12 (b))

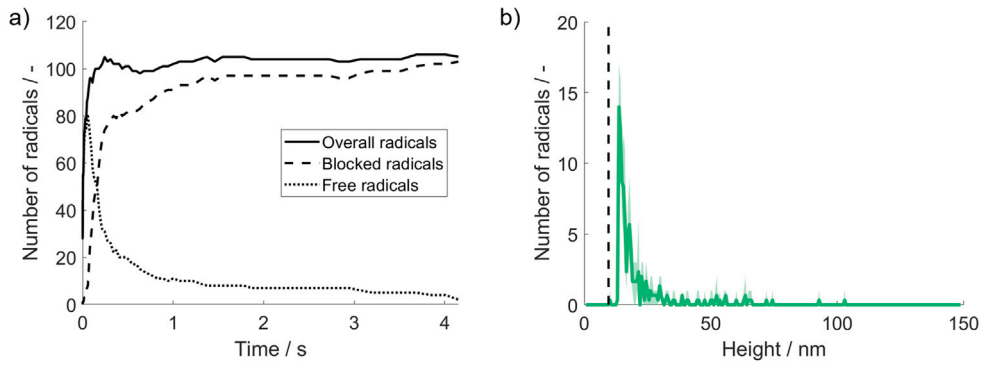

Fig. 5. Number of radicals and reactive chain ends over time and height for an initial SEI thickness of 3.57 nm (case 3, cf. SI). (a) Number of free and blocked radicals, and total number over time. (b) Distribution of radicals over the distance from the electrode after 1 s. The dashed line indicates the lithium metal surface. The solid line represents the average of three independent kMC runs with the same parameter set and corresponding shading shows the maximum observed deviation within these runs.

Table 1
Impact of VC concentration on SEI composition and proportion of consumed VC after 1 s. All values represent the average of three independent runs.

VC concentration/wt.%	2.5	5	7.5	10
Number of Li_2CO_3 / -	6	28.67	27.67	20
Number of LiEDC / -	768.33	624.33	555	474.33
Volume fraction poly(VC) / %	5.1	10.52	11.09	16.39
Consumed VC after 2 μs / %	0.56	0.39	0.35	0.26

and hence acts as a major limiting factor of polymer propagation and thus SEI growth.

Based on this analysis on extended timescales, we can conclude that VC polymerization primarily occurs on timescales starting from milliseconds. As discussed before, it does not affect the very early inorganic SEI formation. However, with increasing surface passivation, the rate of electron transport and subsequent reduction reactions declines, and after approximately 6 ms, polymer propagation reactions become more likely than reduction reactions (cf. SI Fig. 12a). From there on, the further passivation of the surface is mostly chemically driven via propagation instead of electrochemically driven via electrolyte reduction reactions. The major advantage of this is that the chemical propagation does neither consume further active material nor electrolyte species and hence prevents ongoing capacity loss in the cell. Furthermore, polymeric layers were reported to have beneficial properties such as a higher flexibility, which might better accommodate the large volume changes of the lithium metal anode in comparison with non-polymeric SEIs [8,9].

2.4. Impact of electrolyte composition

After discussing the passivating role of the VC additive on SEI formation in the previous Sections, we subsequently analyze if and how the SEI formation is sensitive to the electrolyte composition and could thus be optimized by tailoring the concentrations of the electrolyte.

First, we compare the SEI formation up to 1 s in our standard electrolyte consisting of EC, 1.2M $LiPF_6$ and 5 wt% VC with the binary electrolyte EC:EMC (3:7 by wt.) with 1.2M or 3M $LiPF_6$ and 5 wt%, respectively. As discussed in SI Section 1.5, in this binary electrolyte most EC and VC molecules are expected to be coordinated with at least one Li^+ ion, even at the moderate salt concentration of 1.2M. Therefore, in contrast to the standard electrolyte, the lithiated parameter set (cf. Table 3) is applied for the corresponding calculations. Moreover, EMC is assumed to not significantly contribute to SEI formation.

Fig. 6 illustrates how the chemical composition of the formed SEI changes with the electrolyte composition. As discussed before, in the single-solvent EC electrolyte with 1.2M $LiPF_6$ and 5 wt% VC, we observe a dense layer of LiEDC with few Li_2CO_3, poly(VC) and poly(EC/VC) species, followed by poly(EC/VC) mixed with fewer poly(VC) and some Li_2CO_3. In contrast, in the mixed EC:EMC electrolyte with 1.2M $LiPF_6$ and 5 wt% VC, the formed SEI mostly consists of poly(VC) with very few LiF embedded in the polymer phase close to the surface. Notably, no EC-derived degradation products such as LiEDC, Li_2CO_3 or poly(EC/VC) are observed above the initial passivation layer. This is primarily attributed to the increased ring-opening barrier of lithiated EC species (cf. Table 3, I2), which is applied to all EC molecules in the simulations. It should be noted, that in real systems, a fraction of EC may temporarily remain uncoordinated with Li^+, potentially enabling alternative reaction pathways. An increase of salt concentration from 1.2M to 3M $LiPF_6$ does not significantly alter the chemical SEI composition but leads to a slightly higher amount of the salt-derived product LiF, which is embedded in the polymer phase close to the electrode surface.

Interestingly, the polymer properties and formation dynamics that have been discussed for the standard electrolyte (cf. Section 2.3) are very similar in both mixed electrolytes (cf. SI Fig. 7 - 10): Longer polymer chains just start to form above the millisecond timescale, shorter chains may be found closer to the lithium metal surface, and only few longer chains grow into the electrolyte phase. Moreover, the porosity of the polymeric layer increases with height, and the majority of radical species is found near the anode surface. Across all investigated electrolyte systems, a VC-based polymeric layer forms that passivates the surface and suppresses further electrolyte degradation. These results suggest that VC plays its role as film-forming additive independent of the exact electrolyte composition.

Finally, we analyze the impact of varying VC content in the electrolyte. The overall structure of the SEI, i.e., a compact inner layer consisting of dimers and Li_2CO_3, followed by an outer polymeric layer, remains qualitatively unaffected by VC concentration. The corresponding three-dimensional SEI composition and morphology can be found in the Supplementary Information (cf. SI Fig. 11). However, a number of quantitative differences in SEI composition and growth behavior are observed: First, as displayed in Table 1 the number of EC-derived polymers and oligomers including LiEDC decreases with VC concentration and the volume fraction of poly(VC) within the total polymer phase increases from 5.1% for a VC content of 2.5 wt% to 16.39% for a VC content of 10 wt%. Moreover, the VC concentration impacts properties such as the overall number of polymers, the average polymer chain length and the average SEI thickness. These properties are presented as a function of time and concentration in Fig. 7. For all concentrations, the number of polymers increases steeply within the first milliseconds and stays constant afterwards. Since new polymers are formed only via an electrochemical reduction process (cf. I1 and I2), this clearly shows the quick passivation of the electrode surface within the first few 100 ms. Interestingly, with higher VC concentrations formation of new polymers stops earlier, which indicates a faster surface passivation. This also manifests in the final number of observed polymers after 1 s which is decreasing with VC concentration.

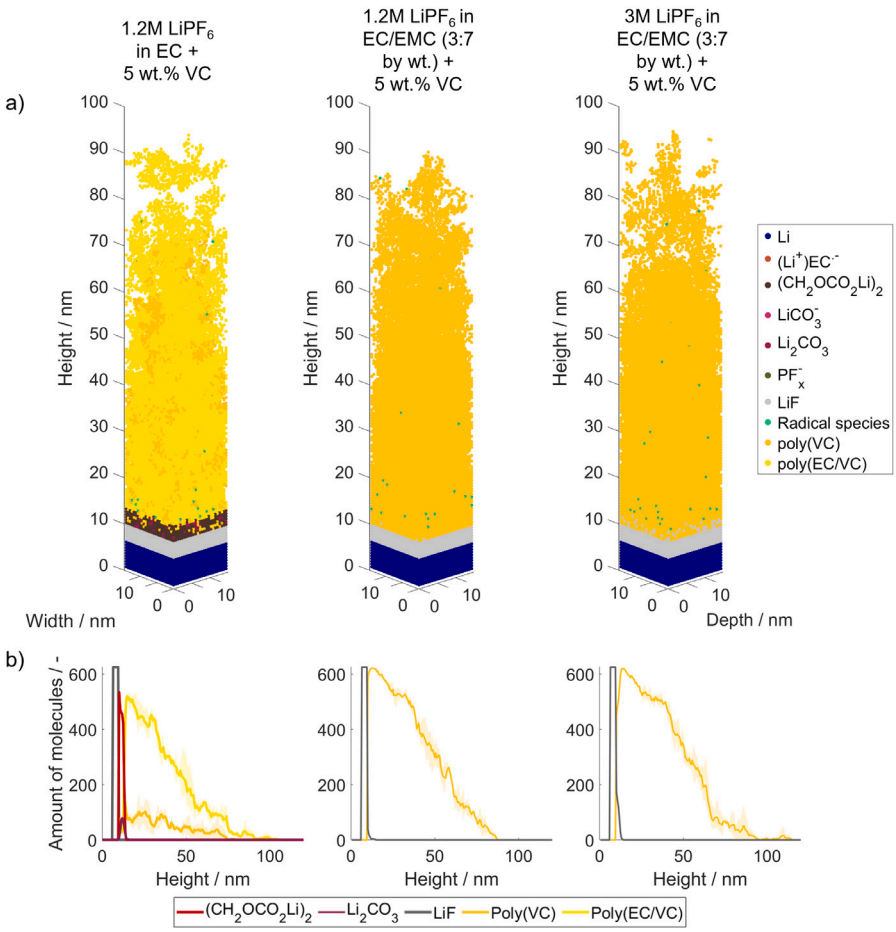

Fig. 6. Chemical composition of SEI formed above the initial LiF passivation layer of 3.57 nm after 1 s in the following three electrolytes: EC + 1.2M $LiPF_6$, EC:EMC (3:7 by wt.) + 1.2M $LiPF_6$ and EC:EMC (3:7 by wt.) + 3M $LiPF_6$, each containing 5 wt% of VC (cases 3, 17, 18, cf. SI). (a) Spatial SEI composition and morphology. (b) SEI composition over height. Solid lines represent the average of three independent kMC runs with the same parameter set, and corresponding shadings show the maximum observed deviation within these runs.

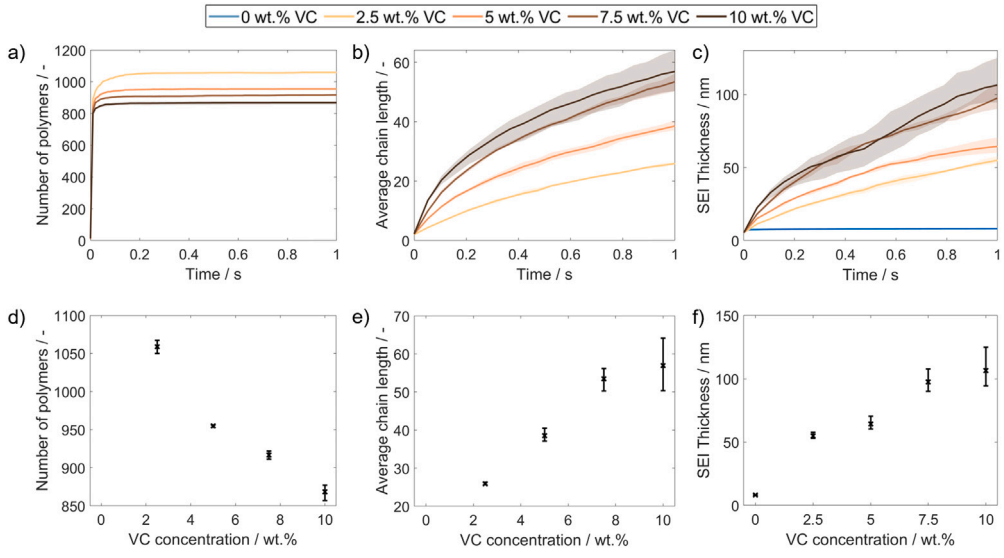

Fig. 7. Impact of VC concentration on SEI formation and properties (cases 7, 11, 12, 13, 14, cf. SI). (a) and (d): Number of formed polymers over time and VC concentration. (b) and (e): Average polymer chain length over time and VC concentration. (c) and (f): Average SEI thickness over time and VC concentration. Solid lines represent the average of three independent kMC runs with the same parameter set and corresponding shadings show the maximum observed deviation within these runs. Concentration dependent properties are shown after 1 s. Data points indicate the average of three independent kMC runs with the same parameter set, and error bars show the maximum observed deviation within these runs.

The average polymer chain length after 1 s of contact between lithium and electrolyte shows the opposite trend and increases with VC concentration. This observation can be attributed to the smaller overall number of polymers present in the SEI as well as to the increased propagation rate due to the higher availability of monomers. This higher propagation rate also causes the higher SEI thickness after 1 s. It can be additionally observed that both, the increase in average polymer chain length and SEI thickness, slow down over time for all analyzed concentrations, which is well in line with our previous analysis of the decreasing number of free radical chain ends. Overall, these results show that changing VC-concentration only slightly affects the formation of the initial layer. The faster surface passivation in case of high VC concentration could be an advantage, since it suppresses unwanted side reactions and reduces the consumption of electrolyte species and active material. However, the resulting increase in SEI thickness may also contribute to higher resistance, as previously reported for VC-based SEI layers [8,9,11,12] and could thus lead to a worse cell performance.

Our simulation further allows to estimate the proportion of VC that was consumed within the first second. Assuming a specific electrolyte volume of roughly 8.6 µl cm^{-2} (cf. SI Section 1.6) between 0.27% (for 10 wt% VC) and 0.56% (for 2.5 wt% VC) of the initial VC molecules has been consumed within the first second (cf. Table 1). Hence, only a small fraction of the additive was consumed within the observed timespan. Since we already observed a deceleration of polymer propagation within this time, we expect that a significant proportion of the additive remains in the electrolyte, which aligns well with previous reports for graphite anodes [62,63]. The remaining additive will then be slowly consumed during cell operation and can quickly repassivate the surface if fresh lithium comes into contact with the electrolyte due to e.g. SEI cracking or dendrite growth. Once all additive has been depleted, this repair mechanism would cease to function, leading to a deteriorating coulombic efficiency and to the end-of-life of the cell. We therefore anticipate that the VC concentration could play a crucial role during cycling, particularly towards the end of the cell's life, although other events such as plating and stripping may substantially alter the scenario [64]. A higher VC concentration is expected to contribute to a longer lifespan, as the additive is depleted more slowly. This hypothesis aligns with experimental reports of extended cycle stability at increased VC concentration [11,65], and may offer a mechanistic explanation for these findings. However, elevated VC concentrations may also lead to an increase in cell internal resistance [9,12,49,65], which could adversely affect rate capability and overall cell performance. This trade-off suggests the existence of an application-dependent optimal VC concentration, which should be subject of future studies.

3. Conclusion

In this study we have presented an ab initio kMC-model with the unique capability of simulating SEI formation on lithium metal up to the macroscopic relevant timescale of seconds. This enabled us to study the impact of VC on the SEI formation with a molecular resolution and to elucidate how it plays its role in enhancing SEI performance and battery lifetime.

The addition of VC has only minor impact on the formation of the initial inorganic SEI within the first microsecond. We attribute this to the initial high reactivity of the lithium metal surface which favors electrochemical reactions and the formation of a high number of dimers over the comparatively slow chemical polymerization process. Only at time scales beyond 1 ms longer polymer chains form. Active chain ends get blocked inside the polymer phase, which slows down the SEI growth over time. These SEI formation dynamics were demonstrated to only slightly be impacted by VC-concentration and electrolyte composition. However, mixed electrolytes favor the formation of a polymer layer that solely consists of poly(VC) chains with embedded LiF clusters, while single-solvent EC with 1.2M $LiPF_6$ result in a mixture of poly(VC) and poly(EC/VC) chains with embedded Li_2CO_3 and a dense LiEDC-rich layer close to the anode surface.

Based on our findings, we attribute the experimentally reported positive impact of VC on SEI and cell performance to a combination of the following factors: First, apart from the initial radical formation, VC-polymerization is a purely chemical process. Therefore, the passivation layer formation in a VC-containing electrolyte proceeds without continuous consumption of solvent, conductive salt or active material. The formed polymeric SEI further prevents ongoing dissolution of electrolyte decomposition products which might further react and cluster in the electrolyte and eventually result in a porous and poorly passivating SEI. Moreover, the observed polymeric SEIs are expected to be more flexible and hence better accommodating towards the drastic volume changes of the lithium anode during operation [8,9,66]. Finally, since only a small fraction of VC is initially consumed, the remaining additive may quickly repair the SEI once new lithium surface becomes exposed to the electrolyte during operation due to e.g. dendrite growth or SEI cracks. In this regard, higher additive concentrations could extend cell lifetime due to slower additive depletion. However, potential increases in internal resistance at elevated concentrations may counteract performance gains, indicating that an optimal balance must be identified in future studies.

Overall, this ab initio informed kMC model provides unique insights by bridging the gap between isolated ab initio reaction mechanisms and their dynamic interplay and shows the resulting structures over extended timescales. The governing VC polymerization processes are suggested to only start to occur above the millisecond timescale, whereas atomistic simulation techniques are limited to the nanosecond-scale and below. This highlights the importance of mesoscale models for understanding the multiscale nature of SEI formation and its interplay with macroscopic properties such as electrolyte composition. Quantitative experimental validation remains challenging due to the molecular resolution and relatively short timescales accessed in the simulations. Nevertheless, the simulation results show qualitative agreement with key experimental trends such as the formation of polymers in VC-containing electrolytes and a layered SEI with more inorganic SEI species close to the electrode and an increasing number of organic species above. To further enhance the predictive power of the presented approach, tailored experiments to specifically validate the predicted SEI structure, e.g. in terms of polymer chain length distribution, would be beneficial. The presented modeling framework can be applied to further liquid electrolyte systems of interest and may hence contribute to a model-assisted electrolyte and SEI design. In the long-term, this knowledge may facilitate the development of rechargeable LMB with improved safety and performance.

4. Methods section

4.1. Density functional theory calculations

DFT was used to calculate the reaction free energy $\Delta_R G_i$ and the energy barriers $\Delta G_i^{\ddagger}$ of the polymer termination reactions. These kinetic parameters were then provided as an input for the subsequent kMC calculations. The molecular modeling was carried out with Gaussian16 [67] in accordance with the previous publication of Kuai and Balbuena [20]. The B3PW91 level of theory with 6-311g(3df) basis sets [68] was used to optimize all structures. Solvation effects were evaluated based on the Solvation Model based on Density (SMD). The catalytic effects of lithium metal were neglected, as direct contact with the electrolyte phase is limited to the initial few nanoseconds of the simulation. Grimme dispersion corrections were included in the calculations. All free energy values were converted to the standard state of 1M.

Table 2
Summary of rate equations for all types of implemented rare events.

Process	Rate equation
Chemical reaction[a]	$\Gamma_{R,i} = k_{0,i} \cdot \exp\left(-\frac{E_{A,i,\mathrm{dir}}}{RT}\right) \cdot \prod_j p_j$
Electrochemical reaction[a]	$\Gamma_{\mathrm{ox},i} = k_{0,i} \cdot \exp\left(-\frac{E_{A,i,\mathrm{dir}}}{RT}\right) \cdot \exp\left(\frac{\alpha F\eta}{RT}\right) \cdot \prod_j p_j$ $\Gamma_{\mathrm{red},i} = \kappa(z) \cdot k_{0,i} \cdot \exp\left(-\frac{E_{A,i,\mathrm{dir}}}{RT}\right) \cdot \exp\left(-\frac{(1-\alpha)F\eta}{RT}\right) \cdot \prod_j p_j$
Transport	$\Gamma_D = \frac{3}{13} \cdot \frac{D}{l^2} \cdot \exp\left(-\frac{E_n}{RT}\right) \cdot \exp\left(-\frac{E_b}{RT}\right)$
Clustering	$\Gamma_{\mathrm{Cl},i} = k_{0,i} \cdot \exp\left(-\frac{E_{A,i}}{RT}\right)$

[a] with dir = {forw, back}.

4.2. Kinetic Monte Carlo model

For this study we used an extended version of the previously introduced 3D-kMC model of Wagner-Henke et al. [34,35]. In the following section we briefly summarize the main model equations with a focus on the model extensions. Our kMC model is based on the Variable Step Size Method [22,25] and a structured list approach according to Schulze [69]. Details on the algorithm can be found in our previous publication [35].

The higher efficiency of kMC approaches compared to atomistic modeling techniques mainly comes from the focus on rare events and the neglection of fast processes such as atomic vibrations [23]. The rare events considered in our model are (electro-)chemical reactions, transport and clustering processes. The respective rate equations of all processes are summarized in Table 2. The description of all symbols may be found in the list of symbols in Table 4. The rates of propagation and termination reactions of polymerization are calculated in the same way as the rates of chemical reactions. In contrast to the implemented non-polymeric species, polymer species can occupy multiple voxels with each subunit occupying one voxel. The same holds for dimers such as LiEDC. Once a macromolecule covers more than one voxel, its transport is neglected since it is considered to be slow compared to the transport of smaller molecules in the electrolyte. Moreover, radical polymer species are assumed to be only reactive at their active chain end. Hence, further propagation and termination reactions can only occur on the voxel, which was added last to the polymer and therefore represents the active site. This approach is very similar to previous kMC polymerization studies such as the work of Arraez et al. [41,42], who applied lattice-based kMC models to investigate surface-initiated polymerization processes. Further assumptions regarding the polymerization processes are that terminated chains cannot be reactivated and that propagation reactions are irreversible.

In the following, further details on the inputs of the rate equations are provided.

The energy barriers for forward and backward reactions are calculated based on the activation energies $\Delta G_i^{\ddagger}$ and reaction energies $\Delta_R G_i$ from DFT as follows:

$$E_{A,i,\mathrm{forw}} = \Delta G_i^{\ddagger} \tag{1}$$

$$E_{A,i,\mathrm{back}} = \Delta G_i^{\ddagger} - \Delta_R G_i \tag{2}$$

Moreover, the electron transport from the lithium metal anode to the site of reaction in the electrolyte is modeled using an electron transport factor $\kappa(z)$:

$$\kappa(z) = \exp\left(-\beta \cdot (z - z_{\mathrm{Li,max}})\right), \quad \text{for } z > z_{\mathrm{Li,max}} \tag{3}$$

Here, β represents the decay factor, $z_{Li,max}$ is the highest position in the kMC box in which lithium metal is present and z is the height variable of the kMC box. Once one layer of lithium metal is entirely consumed, the electron transport factor $\kappa(z)$ is updated, since $z_{Li,max}$ decreases. In literature, exponential decay functions are very common to model electron tunneling [29,31,70]. However, electron tunneling does not reach further than a few nanometers [71,72], and is hence not sufficient to explain experimentally observed SEI thicknesses. Therefore, a number of further electron transport mechanisms through SEI such as electron conduction [73,74], neutral lithium diffusion [16,75] or solvent diffusion through SEI pores is under discussion [71,76]. For simplification, we assume the exponential decay function in Eq. (3) to empirically account for all electron transport processes across the SEI. We do not define a cutoff distance for the exponential decay in this study.

In the transport rate equation Γ_D (cf. Table 2), l represents the diffusion length which equals the size of the lattice sites ΔL in case of face-directed diffusion, $\sqrt{2} \cdot \Delta L$ in case of edge-directed diffusion and $\sqrt{3} \cdot \Delta L$ in case of corner-directed diffusion. Furthermore, the electrostatic energy E_n accounts for repulsive coulombic forces between like-charged neighboring species as given in Eq. (4), which ensures local electroneutrality.

$$E_n = -\frac{N_A}{4 \cdot \pi \cdot \varepsilon_0 \cdot \varepsilon_R \cdot \Delta L} \cdot q_n \cdot \sum q_{nn} \tag{4}$$

Attracting forces are neglected for the sake of computational efficiency and to prevent numerical artifacts which would be caused by the missing long-range interactions of this approach. Hence, E_n is set to 0 if $E_n \geq 0$. In addition, global electroneutrality throughout the entire simulation box is further ensured by coupling each reduction process with the oxidation of lithium metal and the corresponding release of one Li^+-ion. The kMC model does not explicitly account for the effects of the electrical double layer.

Additionally, the second exponential term in the transport rate equation accounts for an additional energy barrier E_b due to adsorption effects of intermediate species on neighboring solid SEI species. Thereby, the local energy barrier is calculated based on the number n_j, type j and binding energy J_j of direct neighbors as shown in Eq. (5).

$$E_b = \sum_j n_j J_j \tag{5}$$

In order to achieve a significant increase of the modeled timescales, we introduce the following new assumptions: First, we introduce implicit electrolyte species, which are assumed to be homogeneously distributed over the empty voxels of the simulation box, for times beyond 2 µs. This is justified as diffusion is significantly faster than reaction at this timescale (SI Section 1.5). These species are not explicitly placed on individual voxels in the simulation box, but can still take part in (electro-)chemical reactions. They may be present on each empty voxel with a probability p_j which is based on their bulk concentration c_j and the lattice site volume ΔL^3 as shown in Eq. (6).

$$p_j = c_j \cdot \Delta L^3 \cdot N_A \tag{6}$$

If implicitly considered species are formed by a reaction, they are not placed in the simulation box, since their concentration is considered to be constant. For explicitly considered species j, p_j is 1 for voxels which are occupied by a molecule of species j, and 0 for voxels which are empty or covered by another species. In addition, the lithium oxidation process is implicitly considered by assuming that the solid transport of lithium atoms in the lithium metal bulk phase is fast enough to fill voids that arise by lithium oxidation. This assumption is based on the self-diffusion coefficient of solid lithium which is reported to be in the range of 4.82 to 7.78 x 10^{-15} m^2 s^{-1} for a temperature of 298 K [77]. Furthermore, we assume that electrolyte decomposition products that are located more than 5 nm away from the upmost layer containing clustered SEI species or lithium metal are dissolved. They are hence removed from the simulation box in order to reduce the number of modeled transport steps of electrolyte decomposition products within the bulk electrolyte phase and to further increase the computational efficiency of the model. This is justified, since interactions with the electrode or SEI surface are not expected beyond this distance.

Table 3
Activation energies in kcal mol^{-1} for VC and EC degradation (I), VC polymerization, cross-polymerization (P) and termination reactions (T) for the lithiated and non-lithiated case. All energies are derived from quantum mechanic calculations. The optional Li^+-coordination is shown in blue.

		$\Delta G_i^{\ddagger}$ / kcal mol^{-1}	
N^0	**Reaction**	**Lithiated**	**Non-lithiated**
I1	$(Li^+)VC + e^- \longleftrightarrow (Li^+)VC^{\bullet-}$	0[c,e]	0[c,e]
I2	$(Li^+)EC + e^- \longleftrightarrow (Li^+)EC^{\bullet-}$	12.05[b]	0[b]
P1	$(Li^+)VC^- + (Li^+)VC \rightarrow (Li^+)poly(VC)_2^{\bullet-}$	9.97[c]	0[c,e]
P2	$(Li^+)poly(VC)_2^{\bullet-} + (Li^+)VC \rightarrow (Li^+)poly(VC)_3^{\bullet-}$	13.54[c]	13.63[c]
P3	$(Li^+)poly(VC)_{n-1}^{\bullet-} + (Li^+)VC \rightarrow (Li^+)poly(VC)_n^{\bullet-}$	14[d]	14[d]
P4	$(Li^+)EC^{\bullet-} + (Li^+)VC \rightarrow (Li^+)poly(EC/VC)_2^{\bullet-}$	13.42[c]	14.31[c]
P5	$(Li^+)poly(EC/VC)_2^{\bullet-} + (Li^+)VC \rightarrow (Li^+)poly(EC/VC)_3^{\bullet-}$	14.1[c]	6.09[c]
P6	$(Li^+)poly(EC/VC)_{n-1}^{\bullet-} + (Li^+)VC \rightarrow (Li^+)poly(EC/VC)_n^{\bullet-}$	14[d]	14[d]
T1	$(Li^+)VC^{\bullet-} + (Li^+)VC^{\bullet-} \rightarrow (Li^+)poly(VC)_2$	0[a,e]	0[a,e]
T2	$(Li^+)VC^{\bullet-} + (Li^+)EC^{\bullet-} \rightarrow (Li^+)poly(EC/VC)_2$	3.97[a]	3.97[a]
T3	$(Li^+)poly(EC/VC)_m^{\bullet-} + (Li^+)poly(EC/VC)_l^{\bullet-} \rightarrow (Li^+)poly(EC/VC)_n$	17.83[a]	17.83[a]
T4	$(Li^+)poly(EC/VC)_m^{\bullet-} + (Li^+)EC^{\bullet-} \rightarrow (Li^+)poly(EC/VC)_n$	16.59[a]	0[a,e]
T5	$(Li^+)poly(EC/VC)_m^{\bullet-} + (Li^+)VC^{\bullet-} \rightarrow (Li^+)poly(EC/VC)_n$	16.78[a]	0[a,e]

[a] Original DFT calculations.
[b] Adopted from Wagner-Henke et al. [35].
[c] Adopted from Kuai and Balbuena [20].
[d] DFT calculations for different Li^+ coordinations were averaged and rounded.
[e] Manually set to 0 kcal mol^{-1} since the DFT calculations suggested negative values.

Table 4
List of Symbols.

Alphabetic	
c_j	Concentration / mol m^{-3}
D	Diffusion coefficient / m^2 s^{-1}
$E_{A,i}$	Energy barrier/kcal mol^{-1}
F	Faraday constant / C mol^{-1}
J_j	Binding energy to species j / kcal mol^{-1}
$k_{0,i}$	Frequency factor / s^{-1}
l	Diffusion length /m
n_j	Number of direct neighbors of type j / -
N_A	Avogadro constant / mol^{-1}
p_j	Site coverage probability for species j / -
q	Charge / A s
R	Ideal gas constant / J mol^{-1} K^{-1}
T	Temperature / K
z	Height coordinate / -
Greek	
α	Symmetry factor / -
β	Electron decay factor / m^{-1}
Γ	Transition rate / s^{-1}
$\Delta G_i^{\ddagger}$	Activation energy of reaction i / kcal mol^{-1}
$\Delta_R G_i$	Gibbs free energy of reaction i / kcal mol^{-1}
ΔL	Distance between lattice sites / m
ϵ_0	Vacuum permittivity / F m^{-1}
ϵ_R	Relative permittivity / -
η	Potential difference / V
κ	Electron transport factor / -
Subscripts/Superscripts	
dir	Direction of reaction
i	Process
j	Species
n	kMC site
nn	Next neighbor

The long-time calculations are further initialized with a primary, simplified SEI layer. This layer can be adjusted to represent the initial passivation due to the SEI formed within the first microsecond and/or further native or artificial passivation layers. It consists of dense LiF, which was chosen, since it constitutes the topmost layer of the primary inorganic SEI (cf. Fig. 1). The Li_2CO_3 layer below is hence not expected to impact follow-up reactions at the SEI/electrolyte interface (cf. SI Fig. 6). The porosity of the primary passivation layer is set to zero, since the short-term calculations indicated a very high density of the LiF-layer in the primary SEI (cf. Fig. 1 (b)). Detailed information on the selection of all parameters is provided in Section 1 of the SI.

4.3. Identification of VC degradation reactions

Our selection of VC degradation and polymerization reactions is based on the study by Kuai and Balbuena [20], in which they identified Gibbs free energies and energy barriers for different VC polymerization, EC polymerization and EC/VC cross-polymerization mechanisms. Based on their results, we selected the suitable VC degradation reactions for our study as follows: First, reasonable reaction mechanisms are expected to have a negative Gibbs free energy $\Delta_R G_i$ to ensure thermodynamic favorability. Second, the corresponding activation energy $\Delta G_i^{\ddagger}$ should be sufficiently low to allow the reaction to proceed in an accessible time. As illustrated exemplarily for a chemical reaction with $k_{0,i} = 10^{13}$ s^{-1} and $p_j = 1$ in SI Fig. 3, the average reaction time until a process occurs is still well below 1 s for an energy barrier of 15 kcal mol^{-1}, significantly increases when it approaches a barrier of 20 kcal mol^{-1} and hits a reaction time of 1000 s for about 21.8 kcal mol^{-1}. Since we do not reach simulation times of up to 1000 s in our kMC simulations, we neglect all reactions with an energy barrier above 21.8 kcal mol^{-1}. Kuai and Balbuena [20] demonstrated that the ring-opening mechanism of VC has to overcome a very high energy barrier of at least 38.48 kcal mol^{-1}. Similarly, both the self-polymerization of EC and its reaction with VC-derived radicals have been reported to exhibit high energy barriers of more than 50 kcal mol^{-1}, respectively. This significantly exceeds our defined cutoff energy barrier of 21.8 kcal mol^{-1}. Therefore, we did not consider these mechanisms for our kMC investigations. In contrast, the calculated energy barriers for the poly(VC) formation mechanism (cf. Scheme 1 (a)) were determined to be well below 21.8 kcal mol^{-1} which makes this reaction mechanism suitable to be studied with our kMC framework (cf. Table 3). The same holds for the cross-polymerization mechanism (cf. Scheme 1 (b)), which is induced by an EC-radical species attacking a VC monomer and followed by subsequent VC polymerization without ring-opening.

Kuai and Balbuena [20] additionally showed that the energy barriers of monomer reduction, initiation and polymerization significantly depend on the lithiation of the monomer and polymer species. Since this lithiation heavily depends on the bulk electrolyte composition (cf. SI Fig. 5), we extracted two different parameter sets from their study as input for our kMC simulation studies. The first one considers all monomers to be coordinated with one Li^+ ion and the second accounts for the case without Li^+-coordination. As demonstrated in our previous work [35], the assumption of lithiated electrolyte molecules aligns well with the local conditions on the lithium metal surface during the initial SEI formation on the nanosecond to microsecond scale. Therefore, the lithiated parameter set is applied for all short-term calculations in this

study. In case of the long-time calculations, we consider a homogeneous bulk electrolyte phase. Hence the amount of lithiated and non-lithiated electrolyte molecules can be estimated (cf. SI Fig. 5). Our calculation shows that in a single-solvent EC electrolyte with 1.2M $LiPF_6$ and 5 wt% VC a high number of non-lithiated electrolyte species exists. Since these are more prone to react compared to their lithiated counterparts (cf. Table 3), the non-lithiated parameter set is used for this case. In contrast, most solvent and additive molecules are coordinated with at least one Li^+ ion in case of a mixed EC:EMC (3:7 by wt.) electrolyte with either 1.2M or 3M $LiPF_6$ and 5 wt% VC (cf. SI Fig. 5). Therefore, the lithiated parameter set is applied for the corresponding calculations.

The summary of the extracted energy barriers can be found in Table 3. Thereby, the energy barriers of the reaction steps I1, I2, P1, P2, P4 and P5 have been directly calculated by DFT. Moreover, all of these steps have negative Gibbs free energies and hence are thermodynamically favorable. Due to computational limitations, the energies for propagation of longer polymer chains (P3 and P6) are not easily accessible by DFT. We therefore make the simplifying assumption that the energy barriers of propagation steps, forming chains longer than three monomers, are independent of the exact chain length and configuration of the polymer species. Hence, the energy barriers of the corresponding polymerization reactions P3 and P6 are set to the next integer values of the respective second propagation steps (P2 and P5). Since all barriers except of the non-lithiated case of P5 are close to 14 kcal mol^{-1}, we set this energy barrier for all long-chain propagation steps. In order to assess the possible impact of this assumption we performed a sensitivity analysis for this parameter (cf. SI Section 2.4). This shows that neither the chemical composition or morphology nor the growth dynamics are highly affected by the exact energy barrier of the long-chain propagation. However, the parameter significantly influences the duration of layer formation, which hence should be interpreted with caution.

The kinetic parameters of the considered termination reactions (cf. Scheme 2) could not be found in literature and were hence calculated using DFT as part of this study. Due to computational limitations of DFT, the termination of the active polymer chains is approximated using the values for the corresponding dimers. Thereby, we assume that the results are also representative for longer polymer chains and that the type of initiator does not have a significant impact on the termination kinetics. All energies were again calculated for a lithiated and a non-lithiated case. The resulting parameters are summarized in Table 3.

CRediT authorship contribution statement

Janika Wagner-Henke: Writing – review & editing, Writing – original draft, Visualization, Project administration, Methodology, Investigation, Funding acquisition, Formal analysis, Data curation, Conceptualization. **Dacheng Kuai:** Writing – review & editing, Writing – original draft, Methodology, Investigation, Formal analysis, Conceptualization. **Perla B. Balbuena:** Writing – review & editing, Supervision, Methodology, Funding acquisition, Formal analysis, Conceptualization. **Ulrike Krewer:** Writing – review & editing, Supervision, Project administration, Funding acquisition, Conceptualization.

Declaration of Generative AI and AI-assisted technologies in the writing process

During the preparation of this work the authors used ChatGPT in order to improve readability and language of the manuscript. After using this tool, the authors reviewed and edited the content as needed and take full responsibility for the content of the published article

Declaration of competing interest

The authors declare that they have no known competing financial interests or personal relationships that could have appeared to influence the work reported in this paper.

Acknowledgments

J.W. and U.K. acknowledge the financial support by the German Federal Ministry of Education and Research, Germany through funding the projects "Lillint and Lillint II – Thermodynamic and kinetic stability of the Lithium-Liquid Electrolyte Interface" (03XP0225F and 03XP0511C). D.K. and P.B.B. acknowledge the Assistant Secretary for Energy Efficiency and Renewable Energy, Office of Vehicle Technologies of the US Department of Energy through the US-Germany Cooperation on Energy Storage, United States under Contract DE-AC02-05CH11357. Computational resources from the Texas A&M University High Performance Research Computing are gratefully acknowledged

Appendix A. Supplementary data

Supplementary material related to this article can be found online at https://doi.org/10.1016/j.ensm.2025.104434.

Data availability

The data presented in this manuscript are openly available in the KITOpen repository under: https://doi.org/10.35097/jyg9f6admdh8a5s2.

References

[1] M. Li, J. Lu, Z. Chen, K. Amine, 30 years of lithium-ion batteries, Adv. Mater. 30 (2018) http://dx.doi.org/10.1002/adma.201800561.
[2] M. Winter, B. Barnett, K. Xu, Before Li ion batteries, Chem. Rev. 118 (2018) 11433–11456, http://dx.doi.org/10.1021/acs.chemrev.8b00422.
[3] A. Bills, S. Sripad, W.L. Fredericks, M. Singh, V. Viswanathan, Performance metrics required of next-generation batteries to electrify commercial aircraft, ACS Energy Lett. 5 (2020) 663–668, http://dx.doi.org/10.1021/acsenergylett.9b02574.
[4] D. Lin, Y. Liu, Y. Cui, Reviving the lithium metal anode for high-energy batteries, Nature Nanotechnology 12 (2017) 194–206, http://dx.doi.org/10.1038/nnano.2017.16.
[5] B. Horstmann, J. Shi, R. Amine, M. Werres, X. He, H. Jia, F. Hausen, I. Cekic-Laskovic, S. Wiemers-Meyer, J. Lopez, D. Galvez-Aranda, F. Baakes, D. Bresser, C.-C. Su, Y. Xu, W. Xu, P. Jakes, R.-A. Eichel, E. Figgemeier, U. Krewer, J.M. Seminario, P.B. Balbuena, C. Wang, S. Passerini, Y. Shao-Horn, M. Winter, K. Amine, R. Kostecki, A. Latz, Strategies towards enabling lithium metal in batteries: interphases and electrodes, Energy Environ. Sci. 14 (2021) 5289–5314, http://dx.doi.org/10.1039/D1EE00767J.
[6] X. He, D. Bresser, S. Passerini, F. Baakes, U. Krewer, J. Lopez, C.T. Mallia, Y. Shao-Horn, I. Cekic-Laskovic, S. Wiemers-Meyer, F.A. Soto, V. Ponce, J.M. Seminario, P.B. Balbuena, H. Jia, W. Xu, Y. Xu, C. Wang, B. Horstmann, R. Amine, C.-C. Su, J. Shi, K. Amine, M. Winter, A. Latz, R. Kostecki, The passivity of lithium electrodes in liquid electrolytes for secondary batteries, Nat. Rev. Mater. 6 (2021) 1036–1052, http://dx.doi.org/10.1038/s41578-021-00345-5.
[7] W. Xu, J. Wang, F. Ding, X. Chen, E. Nasybulin, Y. Zhang, J.G. Zhang, Lithium metal anodes for rechargeable batteries, Energy Environ. Sci. 7 (2014) 513–537, http://dx.doi.org/10.1039/c3ee40795k.
[8] D. Aurbach, K. Gamolsky, B. Markovsky, Y. Gofer, M. Schmidt, U. Heider, On the use of vinylene carbonate (VC) as an additive to electrolyte solutions for Li-ion batteries, Electrochim. Acta 47 (2002) 1423–1439, http://dx.doi.org/10.1016/S0013-4686(01)00858-1.
[9] Y. Xu, H. Wu, Y. He, Q. Chen, J.G. Zhang, W. Xu, C. Wang, Atomic to nanoscale origin of vinylene carbonate enhanced cycling stability of lithium metal anode revealed by cryo-transmission electron microscopy, Nano Lett. 20 (2020) 418–425, http://dx.doi.org/10.1021/acs.nanolett.9b04111.
[10] H. Wu, H. Jia, C. Wang, J.-G. Zhang, W. Xu, Recent progress in understanding solid electrolyte interphase on lithium metal anodes, Adv. Energy Mater. 11 (2021) 2003092, http://dx.doi.org/10.1002/aenm.202003092.

[11] H. Ota, K. Shima, M. Ue, J. ichi Yamaki, Effect of vinylene carbonate as additive to electrolyte for lithium metal anode, Electrochim. Acta 49 (2004) 565–572, http://dx.doi.org/10.1016/j.electacta.2003.09.010.

[12] R. Mogi, M. Inaba, S.-K. Jeong, Y. Iriyama, T. Abe, Z. Ogumi, Effects of some organic additives on lithium deposition in propylene carbonate, J. Electrochem. Soc. 149 (2002) A1578, http://dx.doi.org/10.1149/1.1516770.

[13] F.M. Weber, I. Kohlhaas, E. Figgemeier, Tuning the reactivity of electrolyte solvents on lithium metal by vinylene carbonate, J. Electrochem. Soc. 167 (2020) 140523, http://dx.doi.org/10.1149/1945-7111/abc436.

[14] Y. Wang, S. Nakamura, K. Tasaki, P.B. Balbuena, Theoretical studies to understand surface chemistry on carbon anodes for lithium-ion batteries: How does vinylene carbonate play its role as an electrolyte additive? J. Am. Chem. Soc. 124 (2002) 4408–4421, http://dx.doi.org/10.1021/ja017073i.

[15] Y. Wang, P.B. Balbuena, Theoretical insights into the reductive decompositions of propylene carbonate and vinylene carbonate: Density functional theory studies, J. Phys. Chem. B 106 (2002) 4486–4495, http://dx.doi.org/10.1021/jp014371t.

[16] F.A. Soto, Y. Ma, J.M.M.D.L. Hoz, J.M. Seminario, P.B. Balbuena, Formation and growth mechanisms of solid-electrolyte interphase layers in rechargeable batteries, Chem. Mater. 27 (2015) 7990–8000, http://dx.doi.org/10.1021/acs.chemmater.5b03358.

[17] F. Fasulo, A.B. Muñoz-García, A. Massaro, O. Crescenzi, C. Huang, M. Pavone, Vinylene carbonate reactivity at lithium metal surface: first-principles insights into the early steps of SEI formation, J. Mater. Chem. A 11 (2023) 5660–5669, http://dx.doi.org/10.1039/d2ta08772c.

[18] K. Ushirogata, K. Sodeyama, Z. Futera, Y. Tateyama, Y. Okuno, Near-shore aggregation mechanism of electrolyte decomposition products to explain solid electrolyte interphase formation, J. Electrochem. Soc. 162 (2015) A2670–A2678, http://dx.doi.org/10.1149/2.0301514jes.

[19] K. Ushirogata, K. Sodeyama, Y. Okuno, Y. Tateyama, Additive effect on reductive decomposition and binding of carbonate-based solvent toward solid electrolyte interphase formation in lithium-ion battery, J. Am. Chem. Soc. 135 (2013) 11967–11974, http://dx.doi.org/10.1021/ja405079s.

[20] D. Kuai, P.B. Balbuena, Solvent degradation and polymerization in the li-metal battery: Organic-phase formation in solid-electrolyte interphases, ACS Appl. Mater. Interfaces 14 (2022) 2817–2824, http://dx.doi.org/10.1021/acsami.1c20487.

[21] E.M. Gavilán-Arriazu, M.P. Mercer, D.E. Barraco, H.E. Hoster, E.P.M. Leiva, Kinetic Monte Carlo simulations applied to Li-ion and post Li-ion batteries: a key link in the multi-scale chain, Prog. Energy 3 (4) (2021) 042001, http://dx.doi.org/10.1088/2516-1083/ac1a65.

[22] P. Kratzer, Monte Carlo and kinetic Monte Carlo methods, in: J. Grotendorst, N. Attig, S. Blügel, S.D. Marx (Eds.), Multiscale Simulation Methods in Molecular Science, Jülich Supercomputing Centre, 2009.

[23] M. Andersen, C. Panosetti, K. Reuter, A practical guide to surface kinetic Monte Carlo simulations, Front. Chem. 7 (2019) 1–24, http://dx.doi.org/10.3389/fchem.2019.00202.

[24] G.D. Wehinger, M. Ambrosetti, R. Cheula, Z.B. Ding, M. Isoz, B. Kreitz, K. Kuhlmann, M. Kutscherauer, K. Niyogi, J. Poissonnier, R. Réocreux, D. Rudolf, J. Wagner, R. Zimmermann, M. Bracconi, H. Freund, U. Krewer, M. Maestri, Quo vadis multiscale modeling in reaction engineering? – a perspective, Chem. Eng. Res. Des. 184 (2022) 39–58, http://dx.doi.org/10.1016/j.cherd.2022.05.030.

[25] A.P.J. Jansen, An Introduction to Kinetic Monte Carlo Simulations of Surface Reactions, Springer Berlin Heidelberg, Berlin, Heidelberg, 2012.

[26] C. Hin, Kinetic Monte Carlo simulations of anisotropic lithium intercalation into Li_xFePO_4 electrode nanocrystals, Adv. Funct. Mater. 21 (2011) 2477–2487, http://dx.doi.org/10.1002/adfm.201002049.

[27] N. Sitapure, H. Lee, F. Ospina-Acevedo, P.B. Balbuena, S. Hwang, J.S.I. Kwon, A computational approach to characterize formation of a passivation layer in lithium metal anodes, AIChE J. 67 (2021) 1–11, http://dx.doi.org/10.1002/aic.17073.

[28] R.N. Methekar, P.W.C. Northrop, K. Chen, R.D. Braatz, V.R. Subramanian, Kinetic Monte Carlo simulation of surface heterogeneity in graphite anodes for lithium-ion batteries: Passive layer formation, J. Electrochem. Soc. 158 (2011) A363, http://dx.doi.org/10.1149/1.3548526.

[29] F. Röder, R.D. Braatz, U. Krewer, Multi-scale simulation of heterogeneous surface film growth mechanisms in lithium-ion batteries, J. Electrochem. Soc. 164 (2017) E3335–E3344, http://dx.doi.org/10.1149/2.0241711jes.

[30] F. Röder, V. Laue, U. Krewer, Model based multiscale analysis of film formation in lithium-ion batteries, Batter. Supercaps 2 (2019) 248–265, http://dx.doi.org/10.1002/batt.201800107.

[31] E.W.C. Spotte-Smith, R.L. Kam, D. Barter, X. Xie, T. Hou, S. Dwaraknath, S.M. Blau, K.A. Persson, Toward a mechanistic model of solid–electrolyte interphase formation and evolution in lithium-ion batteries, ACS Energy Lett. 7 (2022) 1446–1453, http://dx.doi.org/10.1021/acsenergylett.2c00517.

[32] M. Esmaeilpour, S. Jana, H. Li, M. Soleymanibrojeni, W. Wenzel, A solution-mediated pathway for the growth of the solid electrolyte interphase in lithium-ion batteries, Adv. Energy Mater. 13 (2023) http://dx.doi.org/10.1002/aenm.202203966.

[33] K. Hankins, M.H. Putra, J. Wagner-Henke, A. Groß, U. Krewer, Insights on SEI Growth and Properties in Na-Ion Batteries via Physically Driven Kinetic Monte Carlo Model, Adv. Energy Mater. 2401153 (2024) 1–13, http://dx.doi.org/10.1002/aenm.202401153.

[34] M. Gerasimov, F.A. Soto, J. Wagner, F. Baakes, N. Guo, F. Ospina-Acevedo, F. Röder, P.B. Balbuena, U. Krewer, Species distribution during solid electrolyte interphase formation on lithium using MD/DFT-Parameterized kinetic Monte Carlo simulations, J. Phys. Chem. C 127 (2023) 4872–4886, http://dx.doi.org/10.1021/acs.jpcc.2c05898.

[35] J. Wagner-Henke, D. Kuai, M. Gerasimov, F. Röder, P.B. Balbuena, U. Krewer, Knowledge-driven design of solid-electrolyte interphases on lithium metal via multiscale modelling, Nat. Commun. 14 (2023) 6823, http://dx.doi.org/10.1038/s41467-023-42212-7.

[36] S.J. An, J. Li, C. Daniel, D. Mohanty, S. Nagpure, D.L. Wood, The state of understanding of the lithium-ion-battery graphite solid electrolyte interphase (SEI) and its relationship to formation cycling, Carbon 105 (2016) 52–76, http://dx.doi.org/10.1016/j.carbon.2016.04.008.

[37] E. Peled, S. Menkin, Review—SEI: Past, present and future, J. Electrochem. Soc. 164 (2017) A1703–A1719, http://dx.doi.org/10.1149/2.1441707jes.

[38] D.R. D'hooge, P.H.M. Van Steenberge, P. Derboven, M.-F. Reyniers, G.B. Marin, Model-based design of the polymer microstructure: bridging the gap between polymer chemistry and engineering, Polym. Chem. 6 (2015) 7081–7096, http://dx.doi.org/10.1039/C5PY01069A.

[39] X.Q. Zhang, R.A.V. Santen, A.P. Jansen, Kinetic Monte Carlo modeling of silicate oligomerization and early gelation, Phys. Chem. Chem. Phys. 14 (2012) 11969–11973, http://dx.doi.org/10.1039/c2cp41194f.

[40] X.-Q. Zhang, T.T. Trinh, R.A.V. Santen, A.P.J. Jansen, Mechanism of the initial stage of silicate oligomerization, J. Am. Chem. Soc. 133 (2011) 6613–6625, http://dx.doi.org/10.1021/ja110357k.

[41] F.J. Arraez, P.H. Van Steenberge, D.R. D'hooge, The competition of termination and shielding to evaluate the success of surface-initiated reversible deactivation radical polymerization, Polymers 12 (2020) http://dx.doi.org/10.3390/polym12061409.

[42] F.J. Arraez, P.H.M. Van Steenberge, D.R. D'hooge, Conformational distributions near and on the substrate during surface-initiated living polymerization: A lattice-based kinetic Monte Carlo approach, Macromolecules 53 (2020) 4630–4648, http://dx.doi.org/10.1021/acs.macromol.0c00585.

[43] L.D. Gibson, J. Pfaendtner, Solvent oligomerization pathways facilitated by electrolyte additives during solid-electrolyte interphase formation, Phys. Chem. Chem. Phys. 22 (2020) 21494–21503, http://dx.doi.org/10.1039/d0cp03286g.

[44] Y. Kamikawa, K. Amezawa, K. Terada, First-principles study on the mechanical properties of polymers formed by the electrochemical reduction of fluoroethylene carbonate and vinylene carbonate, J. Phys. Chem. C 124 (2020) 19937–19944, http://dx.doi.org/10.1021/acs.jpcc.0c04878.

[45] L.E. Ouatani, R. Dedryvère, C. Siret, P. Biensan, S. Reynaud, P. Iratçabal, D. Gonbeau, The effect of vinylene carbonate additive on surface film formation on both electrodes in Li-ion batteries, J. Electrochem. Soc. 156 (2009) A103, http://dx.doi.org/10.1149/1.3029674.

[46] A.L. Michan, B.S. Parimalam, M. Leskes, R.N. Kerber, T. Yoon, C.P. Grey, B.L. Lucht, Fluoroethylene carbonate and vinylene carbonate reduction: Understanding lithium-ion battery electrolyte additives and solid electrolyte interphase formation, Chem. Mater. 28 (2016) 8149–8159, http://dx.doi.org/10.1021/acs.chemmater.6b02282.

[47] M. Nie, J. Demeaux, B.T. Young, D.R. Heskett, Y. Chen, A. Bose, J.C. Woicik, B.L. Lucht, Effect of vinylene carbonate and fluoroethylene carbonate on SEI formation on graphitic anodes in li-ion batteries, J. Electrochem. Soc. 162 (2015) A7008–A7014, http://dx.doi.org/10.1149/2.0021513jes.

[48] B. Zhang, M. Metzger, S. Solchenbach, M. Payne, S. Meini, H.A. Gasteiger, A. Garsuch, B.L. Lucht, Role of 1,3-propane sultone and vinylene carbonate in solid electrolyte interface formation and gas generation, J. Phys. Chem. C 119 (2015) 11337–11348, http://dx.doi.org/10.1021/acs.jpcc.5b00072.

[49] H. Ota, Y. Sakata, A. Inoue, S. Yamaguchi, Analysis of vinylene carbonate derived SEI layers on graphite anode, J. Electrochem. Soc. 151 (2004) A1659, http://dx.doi.org/10.1149/1.1785795.

[50] P. Sayavong, W. Zhang, S.T. Oyakhire, D.T. Boyle, Y. Chen, S.C. Kim, R.A. Vilá, S.E. Holmes, M.S. Kim, S.F. Bent, Z. Bao, Y. Cui, Dissolution of the solid electrolyte interphase and its effects on lithium metal anode cyclability, J. Am. Chem. Soc. 145 (2023) 12342–12350, http://dx.doi.org/10.1021/jacs.3c03195.

[51] S.M. Wood, C. Fang, E.J. Dufek, S.C. Nagpure, S.V. Sazhin, B. Liaw, Y.S. Meng, Predicting calendar aging in lithium metal secondary batteries: The impacts of solid electrolyte interphase composition and stability, Adv. Energy Mater. 8 (2018) 1–6, http://dx.doi.org/10.1002/aenm.201801427.

[52] D.T. Boyle, W. Huang, H. Wang, Y. Li, H. Chen, Z. Yu, W. Zhang, Z. Bao, Y. Cui, Corrosion of lithium metal anodes during calendar ageing and its microscopic origins, Nat. Energy 6 (2021) 487–494, http://dx.doi.org/10.1038/s41560-021-00787-9.

[53] S.-K. Otto, Y. Moryson, T. Krauskopf, K. Peppler, J. Sann, J. Janek, A. Henss, In-depth characterization of lithium-metal surfaces with XPS and ToF-SIMS: Toward better understanding of the passivation layer, Chem. Mater. 33 (2021) 859–867, http://dx.doi.org/10.1021/acs.chemmater.0c03518.

[54] J. Wellmann, J.P. Brinkmann, B. Wankmiller, K. Neuhaus, U. Rodehorst, M.R. Hansen, M. Winter, E. Paillard, Effective solid electrolyte interphase formation on lithium metal anodes by mechanochemical modification, ACS Appl. Mater. Interfaces 13 (2021) 34227–34237, http://dx.doi.org/10.1021/acsami.1c07490.

[55] K. Thanner, A. Varzi, D. Buchholz, S.J. Sedlmaier, S. Passerini, Artificial solid electrolyte interphases for lithium metal electrodes by wet processing: The role of metal salt concentration and solvent choice, ACS Appl. Mater. Interfaces 12 (2020) 32851–32862, http://dx.doi.org/10.1021/acsami.0c08938.

[56] M. He, R. Guo, G.M. Hobold, H. Gao, B.M. Gallant, The intrinsic behavior of lithium fluoride in solid electrolyte interphases on lithium, Proc. Natl. Acad. Sci. 117 (2020) 73–79, http://dx.doi.org/10.1073/pnas.1911017116.

[57] J. Genzer, In silico polymerization: Computer simulation of controlled radical polymerization in bulk and on flat surfaces, Macromolecules 39 (2006) 7157–7169, http://dx.doi.org/10.1021/ma061155f.

[58] H. Liu, Y.L. Zhu, J. Zhang, Z.Y. Lu, Z.Y. Sun, Influence of grafting surface curvature on chain polydispersity and molecular weight in concave surface-initiated polymerization, ACS Macro Lett. 1 (2012) 1249–1253, http://dx.doi.org/10.1021/mz3003374.

[59] E. Mastan, L. Xi, S. Zhu, Factors affecting grafting density in surface-initiated ATRP: A simulation study, Macromol. Theory Simul. 25 (2016) 220–228, http://dx.doi.org/10.1002/mats.201500081.

[60] P. Polanowski, J.K. Jeszka, K. Matyjaszewski, Polymer brushes in pores by ATRP: Monte Carlo simulations, Polymer 211 (2020) 123124, http://dx.doi.org/10.1016/j.polymer.2020.123124.

[61] Y.N. Zhou, J.J. Li, T.T. Wang, Y.Y. Wu, Z.H. Luo, Precision polymer synthesis by controlled radical polymerization: Fusing the progress from polymer chemistry and reaction engineering, Prog. Polym. Sci. 130 (2022) 101555, http://dx.doi.org/10.1016/j.progpolymsci.2022.101555.

[62] R. Stockhausen, L. Gehrlein, M. Müller, T. Bergfeldt, A. Hofmann, F.J. Müller, J. Maibach, H. Ehrenberg, A. Smith, Investigating the dominant decomposition mechanisms in lithium-ion battery cells responsible for capacity loss in different stages of electrochemical aging, J. Power Sources 543 (2022) 231842, http://dx.doi.org/10.1016/j.jpowsour.2022.231842.

[63] M. Leißing, F. Horsthemke, S. Wiemers-Meyer, M. Winter, P. Niehoff, S. Nowak, The impact of the C-rate on gassing during formation of NMC622 II graphite lithium-ion battery cells, Batter. Supercaps 4 (2021) 1344–1350, http://dx.doi.org/10.1002/batt.202100056.

[64] S. Perez-Beltran, D. Kuai, P.B. Balbuena, SEI formation and lithium-ion electrodeposition dynamics in lithium metal batteries via first-principles kinetic Monte Carlo modeling, ACS Energy Lett. 9 (2024) 5268–5278, http://dx.doi.org/10.1021/acsenergylett.4c02019.

[65] Z.L. Brown, S. Jurng, B.L. Lucht, Investigation of the lithium solid electrolyte interphase in vinylene carbonate electrolytes using Cu||$LiFePO_4$ cells, J. Electrochem. Soc. 164 (2017) A2186–A2189, http://dx.doi.org/10.1149/2.0021712jes.

[66] X. Ren, Y. Zhang, M.H. Engelhard, Q. Li, J.G. Zhang, W. Xu, Guided lithium metal deposition and improved lithium Coulombic efficiency through synergistic effects of $LiAsF_6$ and cyclic carbonate additives, ACS Energy Lett. 3 (2018) 14–19, http://dx.doi.org/10.1021/acsenergylett.7b00982.

[67] M.J. Frisch, G.W. Trucks, H.B. Schlegel, G.E. Scuseria, M.A. Robb, J.R. Cheeseman, G. Scalmani, V. Barone, G.A. Petersson, Gaussian 16 Revision C.01, Gaussian Inc., Wallingford CT, 2016.

[68] R. Krishnan, J.S. Binkley, R. Seeger, J.A. Pople, Self-consistent molecular orbital methods. XX. A basis set for correlated wave functions, J. Chem. Phys. 72 (1980) 650–654, http://dx.doi.org/10.1063/1.438955.

[69] T.P. Schulze, Kinetic Monte Carlo simulations with minimal searching, Phys. Rev. E - Stat. Phys. Plasmas, Fluids, Relat. Interdiscip. Top. 65 (2002) 1–3, http://dx.doi.org/10.1103/PhysRevE.65.036704.

[70] D. Li, D. Danilov, Z. Zhang, H. Chen, Y. Yang, P.H.L. Notten, Modeling the SEI-formation on graphite electrodes in $LiFePO_4$ batteries, J. Electrochem. Soc. 162 (2015) A858–A869, http://dx.doi.org/10.1149/2.0161506jes.

[71] M. Tang, S. Lu, J. Newman, Experimental and theoretical investigation of solid-electrolyte-interphase formation mechanisms on glassy carbon, J. Electrochem. Soc. 159 (2012) A1775–A1785, http://dx.doi.org/10.1149/2.025211jes.

[72] L. Kolzenberg, A. Latz, B. Horstmann, Solid–electrolyte interphase during battery cycling: Theory of growth regimes, ChemSusChem 13 (2020) 3901–3910, http://dx.doi.org/10.1002/cssc.202000867.

[73] M. Broussely, S. Herreyre, P. Biensan, P. Kasztejna, K. Nechev, R.J. Staniewicz, Aging mechanism in li ion cells and calendar life predictions, J. Power Sources 97–98 (2001) 13–21, http://dx.doi.org/10.1016/S0378-7753(01)00722-4.

[74] F. Single, B. Horstmann, A. Latz, Revealing SEI morphology: In-depth analysis of a modeling approach, J. Electrochem. Soc. 164 (2017) E3132–E3145, http://dx.doi.org/10.1149/2.0121711jes.

[75] S. Shi, P. Lu, Z. Liu, Y. Qi, L.G. Hector, H. Li, S.J. Harris, Direct calculation of Li-ion transport in the solid electrolyte interphase, J. Am. Chem. Soc. 134 (2012) 15476–15487, http://dx.doi.org/10.1021/ja305366r.

[76] F. Single, B. Horstmann, A. Latz, Dynamics and morphology of solid electrolyte interphase (SEI), Phys. Chem. Chem. Phys. 18 (2016) 17810–17814, http://dx.doi.org/10.1039/c6cp02816k.

[77] E. Dologlou, Self-diffusion in solid lithium, Glas. Phys. Chem. 36 (2010) 570–574, http://dx.doi.org/10.1134/S1087659610050056.